



Deposited via The University of Leeds.

White Rose Research Online URL for this paper:

<https://eprints.whiterose.ac.uk/id/eprint/167617/>

Version: Accepted Version

---

**Article:**

Liu, Y, Magnall, JM, Gleeson, SA et al. (2020) Spatio-temporal evolution of ocean redox and nitrogen cycling in the early Cambrian Yangtze ocean. *Chemical Geology*. ISSN: 0009-2541

<https://doi.org/10.1016/j.chemgeo.2020.119803>

---

© 2020, Elsevier. This manuscript version is made available under the CC-BY-NC-ND 4.0 license <http://creativecommons.org/licenses/by-nc-nd/4.0/>.

**Reuse**

This article is distributed under the terms of the Creative Commons Attribution-NonCommercial-NoDerivs (CC BY-NC-ND) licence. This licence only allows you to download this work and share it with others as long as you credit the authors, but you can't change the article in any way or use it commercially. More information and the full terms of the licence here: <https://creativecommons.org/licenses/>

**Takedown**

If you consider content in White Rose Research Online to be in breach of UK law, please notify us by emailing [eprints@whiterose.ac.uk](mailto:eprints@whiterose.ac.uk) including the URL of the record and the reason for the withdrawal request.

# 1 Spatio-temporal evolution of ocean redox 2 and nitrogen cycling in the early Cambrian 3 Yangtze ocean

4  
5 Yang Liu<sup>a, b\*</sup>, Joseph M. Magnall<sup>b</sup>, Sarah A. Gleeson<sup>b, c</sup>, Frederick  
6 Bowyer<sup>d</sup>, Simon W. Poulton<sup>d</sup>, Jinchuan Zhang<sup>a</sup>

7 <sup>a</sup> School of Energy resource, China University of Geosciences (Beijing),  
8 Beijing 100083, China.

9 <sup>b</sup> GFZ German Research Centre for Geosciences, 14473 Potsdam, Germany.

10 <sup>c</sup> Institute of Geological Sciences, Freie Universität, 74-100 Malteserstrasse,  
11 Berlin 12249, Germany.

12 <sup>d</sup> School of Earth and Environment, University of Leeds, Leeds LS2 9JT, UK.

13 Corresponding Author: [yanqliu@cugb.edu.cn](mailto:yanqliu@cugb.edu.cn)

14

## 15 **Abstract**

16 The early Cambrian was a critical interval for the Earth system, during which  
17 a rise in oceanic and atmospheric oxygen levels coincided with the rapid  
18 diversification of metazoans. A variety of contrasting models have been  
19 proposed for the spatiotemporal redox evolution of the early Cambrian ocean.  
20 These include the development of a well-oxygenated deep ocean at the base  
21 of Cambrian Stage 3 (commencing at ~521 Ma), or alternatively, persistent  
22 and widespread anoxic (ferruginous) conditions throughout the early Cambrian

23 ocean. Here, we present redox sensitive trace element (RSTE), Fe speciation,  
24 and N and C isotope ( $\delta^{15}\text{N}_{\text{sed}}$  and  $\delta^{13}\text{C}_{\text{org}}$ ) data for samples from a section  
25 (Zhongnancun) of the early Cambrian Niutitang Formation, which was  
26 deposited on the outer-shelf of the Yangtze Block, South China. The Fe  
27 speciation and RSTE data provide evidence of a transition from euxinic,  
28 through ferruginous, to oxic conditions during deposition of the Niutitang  
29 Formation. The combination of these new data with existing data from the  
30 inner-shelf to basin environment, implies regional redox stratification across  
31 the Yangtze Block during Cambrian stages 2 and 3, with oxic shallow waters  
32 above ferruginous deep waters, and spatial variability in the degree of  
33 mid-depth euxinia. Oxygenation of deeper waters may have occurred by early  
34 Cambrian Stage 4 (~514 Ma). A compilation of  $\delta^{15}\text{N}$  values from multiple early  
35 Cambrian sections of the Yangtze Block indicate that  $\text{N}_2$  fixation dominated the  
36 nitrogen cycle during late Cambrian Stage 2. Low  $\delta^{15}\text{N}$  values ( $< -2\text{‰}$ )  
37 preserved in shelf sections can be interpreted to represent partial assimilation  
38 of  $\text{NH}_4^+$ , where  $\text{NH}_4^+$  was not a limiting nutrient. During the early-middle  
39 Cambrian Stage 3, more positive  $\delta^{15}\text{N}$  values (0 to  $+3\text{‰}$ ) are recorded in shelf  
40 sections, with lower values ( $-2$  to  $+2\text{‰}$ ) recorded in slope-basin sections. The  
41 positive  $\delta^{15}\text{N}$  values observed in shelf sections are likely a consequence of  
42 partial denitrification in the water column, whereas coeval deeper water  $\delta^{15}\text{N}$   
43 values of  $\sim 0\text{‰}$  may reflect the dominance of  $\text{N}_2$  fixation. The distribution of  
44  $\delta^{15}\text{N}$  values, combined with a gradient in  $\delta^{13}\text{C}_{\text{org}}$  values, are consistent with a

45 stratified ocean model. The  $\delta^{15}\text{N}$  values of all sections are lower than those of  
46 the modern ocean, which may indicate that the nitrate concentration of the  
47 early Cambrian Yangtze ocean was generally low during Cambrian Stage 3.  
48 The observed gradient in  $\delta^{15}\text{N}$  values is similar to that observed in records  
49 from Mesoproterozoic oceans, suggesting that abundant nitrate availability  
50 may have been restricted to shelf environments. We propose that increased  
51 nitrogen availability in shelf settings may have contributed to the evolution of  
52 large-celled eukaryotic phytoplankton. This provided a positive feedback on  
53 ocean oxygenation, allowing for increased complexity in early animal  
54 ecosystems on the continental shelf, and ultimately deep water oxygenation.

55

56 **Key words:** Nitrogen isotopes; Redox conditions; Nitrogen cycle; Early  
57 Cambrian; South China.

58

## 59 **1. Introduction**

60 The early Cambrian (~529 - 514 Ma, late Fortunian to early Stage 4)  
61 encompasses an interval of major evolutionary innovation, including the rapid  
62 diversification of crown group Metazoa, against a backdrop of global climatic  
63 instability and variability in the chemical composition of the oceans and  
64 atmosphere (Krause et al., 2018; He et al., 2019; Wood et al., 2019). Perhaps  
65 most significantly, Cambrian Stage 3 in South China includes the radiation of  
66 crown group bilateria and non-bilateria, alongside preservation of the

67 Chengjiang Lagerstätte ([Wood et al., 2019](#)). This interval also immediately  
68 precedes the global Sinsk extinction event ([Zhuravlev and Wood, 1996](#); [He et](#)  
69 [al., 2019](#)).

70 The number of studies attempting to more precisely constrain the spatial and  
71 temporal redox evolution of the early Cambrian ocean has increased in recent  
72 years. Multiple studies have focused on platform to basin reconstructions of  
73 the Yangtze Block (South China) with integrated sequence stratigraphy,  
74 resulting in broad spatial constraints on the redox evolution of these  
75 depositional environments. During the early Cambrian there is widespread  
76 evidence for anoxic ferruginous conditions, as constrained by a number of  
77 different proxies, including Fe speciation ([Goldberg et al., 2007](#); [Canfield et al.,](#)  
78 [2008](#); [Och et al., 2016](#); [Li et al. 2017](#); [Hammarlund et al., 2017](#)),  
79 redox-sensitive trace elements ([Xu et al., 2012](#); [Jin et al., 2016](#)), and sulfur  
80 isotope compositions ([Feng et al., 2014](#)). A stepwise expansion of oxic water  
81 column conditions from shallow to deep settings is then recorded across the  
82 Yangtze Block through Cambrian Stages 2 to 4, albeit with continued evidence  
83 for locally ferruginous conditions in deeper water settings ([Li et al. 2017](#);  
84 [Hammarlund et al., 2017](#)). The preservation of near-modern seawater  $\delta^{98/95}\text{Mo}$   
85 values ( $\sim 2.34\text{‰}$ ) recorded in black shales, however, has been used as  
86 evidence of an expanded oxic sink for Mo in the global oceans by Cambrian  
87 Stage 3 ( $\sim 521$  Ma, [Chen et al., 2015](#); [Wen et al., 2015](#)). [Wang et al. \(2018\)](#)  
88 suggested that oxygenation of the deep ocean occurred during Cambrian

89 Stage 3, based on a comprehensive N isotope dataset from the Yangtze Block.

90 One of the main challenges associated with interpreting geochemical redox  
91 proxies relates to discriminating between local and global conditions, and  
92 combining both temporal and spatial variability. Recently, geochemical and  
93 paleontological data from multiple stratigraphic sections were integrated in a  
94 sequence stratigraphic framework to reconstruct spatio-temporal redox  
95 evolution along a Cambrian basin margin sequence from the Baltic Sea  
96 (Guilbaud et al. 2018). In their study, Guilbaud et al. (2018) argued for the  
97 development of an oxygen minimum zone (OMZ) along a productive  
98 continental margin. A euxinic wedge could be dynamically maintained above  
99 deeper ferruginous waters, if sufficient sulfate and organic matter were  
100 available (Poulton et al., 2010; Poulton and Canfield, 2011; Li et al., 2018). The  
101 OMZ model has also been applied to stratigraphic sequences from the  
102 Yangtze Block (e.g. Hammarlund et al. 2017). However, there has been limited  
103 evaluation as to the spatial extent of this redox architecture across the Yangtze  
104 Block, or higher order stratification with respect to intermediate redox states (in  
105 addition to oxic, anoxic and euxinic conditions). For example, aerobic  
106 conditions in the surface ocean may have overlain deeper nitrogenous waters,  
107 with manganoous (Tostevin et al., 2016) and then ferruginous water column  
108 conditions below, as electron acceptors were utilized in order of their energy  
109 yield during organic carbon remineralization.

110 Iron speciation (Poulton and Canfield, 2005) is a particularly robust proxy

111 used for reconstructing local depositional redox conditions (e.g., [Poulton et al.,](#)  
112 [2004; Canfield et al., 2007; Poulton and Canfield, 2011](#)). When combined with  
113 redox-sensitive trace element (RSTE) concentrations and ratios ([Tribovillard et](#)  
114 [al., 2006; Algeo and Rowe, 2012](#)), a detailed characterisation of the precise  
115 nature of ocean redox chemistry can be achieved. In addition, nitrogen  
116 isotopes ( $\delta^{15}\text{N}$ ) are sensitive to productivity in the photic zone, and the isotopic  
117 signature of biomass produced in the photic zone may ultimately be preserved  
118 in sediments. The redox structure of the ocean exerts a strong control on the  
119 speciation of dissolved inorganic nitrogen, with  $\text{NO}_3^-$  being stable in oxic  
120 waters and  $\text{NH}_4^+$  being stable in anoxic waters ([Ader et al., 2016](#)). As such,  
121  $\delta^{15}\text{N}$  values are increasingly being utilized in studies of seawater paleoredox in  
122 both the Phanerozoic and Precambrian (e.g. [Algeo et al., 2008; Godfrey and](#)  
123 [Falkowski, 2009; Higgins et al., 2012; Godfrey et al., 2013; Stüeken, 2013;](#)  
124 [Ader et al., 2016; Stüeken et al., 2016; Zerkle et al., 2017](#)).

125 In this study, we report Fe speciation, RSTE,  $\delta^{15}\text{N}_{\text{sed}}$  and  $\delta^{13}\text{C}_{\text{org}}$  values from  
126 a new outer-shelf outcrop section of Cambrian stratigraphy from the Yangtze  
127 Block. We compile our new data with previously published data from  
128 correlative sections, to present a more comprehensive model for the spatial  
129 and temporal evolution of nitrogen cycling in the early Cambrian Yangtze  
130 ocean. Subsequently, we evaluate possible links between nitrogen availability,  
131 marine paleoredox and biological evolution during this key interval of Earth  
132 history.

133

## 134 **2. Geological setting**

135 Neoproterozoic and early Cambrian marine sedimentary rocks are well  
136 preserved in the Yangtze Block, South China. According to palaeomagnetic  
137 records, South China was at low-latitudes during the early Cambrian ([Merdith  
138 et al., 2017](#)). Paleogeographic reconstructions show that the environmental  
139 setting of the Yangtze Block comprised platform facies, a transition zone, and  
140 slope to basin facies, as illustrated in [Fig. 1](#) ([Steiner et al., 2001](#); [Jiang et al.,  
141 2012](#)). The lower Cambrian Niutitang Formation and equivalent strata  
142 unconformably overly the upper Ediacaran Dengying Formation. The  
143 Niutitang Formation is dominantly comprised of black shale, but the lower  
144 parts of the Formation contain bedded phosphorite, barite, and thick units (up  
145 to tens of meters) of "stone coal" (combustible shale of algal origin, [Xu et al.,  
146 2012](#)). Furthermore, in Guizhou and Hunan Province, an organic-rich, Ni-Mo  
147 sulfide layer with a maximum thickness of 30 cm is used as a marker horizon  
148 for the lowermost part of the Niutitang Formation ([Jiang et al., 2006](#); [Xu et al.,  
149 2012](#)). Previous studies have evaluated the thermal maturity of organic matter  
150 to show the Niutitang Formation has only undergone sub-greenschist  
151 (prehnite-pumpellyite) facies metamorphism ([Křibek et al., 2007](#)).

152 The Zhongnancun section in this study is located in Zunyi city, Guizhou  
153 province (N 27°41'21.4", E 106°40'67.0"), and paleo-geographically lies in the  
154 transition zone (outer-shelf) ([Fig. 1](#), [Pi et al., 2013](#)). The Niutitang Formation

155 at this section has been divided into 3 intervals according to lithostratigraphic  
156 analysis. Interval 1 contains a variety of rock types, including brownish to  
157 black, siliceous phosphorite (~65 cm in thickness), a K-bentonite layer  
158 interbedded with black chert (~20 cm in thickness), carbonaceous chert  
159 interbedded with black shale (~1.70 m in thickness), and carbonaceous shale  
160 (~2.90 m in thickness). The K-bentonite layer at the Zhongnancun section has  
161 been dated using the SHRIMP U-Pb method to  $532.3 \pm 0.7$  Ma (Jiang et al.,  
162 2009). The phosphorite deposits and nodules hosted by Lower Cambrian  
163 shale across the Yangtze Block may have resulted from the interaction of  
164 upwelling P-replete water with oxygenated surface waters (Wille et al., 2008).  
165 The origin of the widespread Ediacaran-Cambrian (E-C) chert deposits in the  
166 Yangtze block has recently been revealed by silicon isotopes, indicating that  
167 seawater was the primary silica source of the cherts (Gao et al., 2020).

168 The base of Interval 2 is marked by the aforementioned Ni-Mo sulfide layer  
169 (~15 cm thick), which is considered to belong to Cambrian Stage 2 based on  
170 biostratigraphic data (Steiner et al., 2001). A Re-Os isochron age of  $521 \pm 5$   
171 Ma has been reported for the sulfide ore from three mining sites (Sancha in  
172 Hunan province, and Dazhuliushui and Maluhe in Guizhou province) (Xu et al.,  
173 2011), confirming the biostratigraphic age. The Ni-Mo sulfide layer is  
174 considered to have been deposited under euxinic conditions (Lehmann et al.,  
175 2007; Steiner et al., 2001) but the origin of the metal enrichment is debated.  
176 Previous studies have suggested that the sulfide layer may be a product of

177 hydrothermal venting (Steiner et al., 2001; Jiang et al., 2006) versus  
178 scavenging from seawater by organic matter (Lehmann et al., 2007; Xu et al.,  
179 2011). The potential effects of volcanic input on early Cambrian black shale  
180 and sulfide ore of South China has been indicated by mercury isotopes,  
181 suggesting that Hg in these rocks mainly originated from seawater (Yin et al.,  
182 2017). The remainder of Interval 2 consists of ~16 m of black shale, overlain  
183 by Interval 3, which is dominated by dark gray to black silty shale with a  
184 thickness of ~12 m.

185

### 186 **3. Materials and methods**

187 A total of 39 samples (~1 kg each) were collected from the lower Cambrian  
188 Niutitang Formation at the Zhongnancun outcrop section, including three chert  
189 samples, one sulfide ore sample and 35 shale samples. These samples were  
190 carefully trimmed to remove possible weathered surfaces. Approximately 300  
191 – 500 g of remaining material from each sample was then crushed to a fine  
192 powder (<74  $\mu\text{m}$ ) using an agate mortar.

193 Total organic carbon (TOC) concentrations were determined on a LECO  
194 CS-230 carbon and sulfur analyzer at the Geochemistry Laboratory of Yangtze  
195 University. Prior to analysis, samples were subjected to a pre-leach in 6 M HCl  
196 for 24 hrs, in order to remove carbonate. Major and trace elements were  
197 analyzed using XRF (AB104L, AL104, AxiosmAX) and ICP-MS (PerkinElmer,  
198 Elan DCR-e), respectively, at the Beijing Research Institute of Uranium

199 Geology. Detailed descriptions of the methods have been published by [Gao et](#)  
200 [al. \(2015\)](#). For ICP-MS analysis, approximately 50 mg of powdered samples  
201 were treated with a solution mixture of 2 ml HNO<sub>3</sub>, 3 ml HF and 1 ml HCl at  
202 150°C. After drying, the residues were treated with 1 ml HNO<sub>3</sub> and 3 ml HF at  
203 180°C for 48 h. After samples were dissolved, each solution was cooled and  
204 0.5 ml HClO<sub>4</sub> (70%) was used to oxidize organic matter. After evaporation,  
205 residues were re-dissolved in 2 ml HNO<sub>3</sub> for analysis. Analytical errors are  
206 generally better than 10% for Fe<sub>T</sub> and Al, and ±5% for trace elements. Trace  
207 metal enrichment factors (Mo<sub>EF</sub> and U<sub>EF</sub>) were calculated using the formula:  
208  $X_{EF} = (X/Al)_{\text{sample}} / (X/Al)_{\text{AUCC}}$ , where X = Mo or U, and AUCC refers to the  
209 composition of average upper continental crust ([McLennan, 2001](#)).

210 Iron speciation was conducted to reconstruct water column palaeoredox  
211 conditions. Highly reactive iron (Fe<sub>HR</sub>) was determined as the sum of four  
212 operationally-defined pools, predominantly comprising pyrite Fe (Fe<sub>py</sub>),  
213 carbonate-associated Fe (Fe<sub>carb</sub>), ferric oxide Fe (Fe<sub>ox</sub>), and magnetite Fe  
214 (Fe<sub>mag</sub>) ([Poulton et al., 2004](#); [Poulton and Canfield, 2011](#)). Fe<sub>carb</sub>, Fe<sub>ox</sub> and  
215 Fe<sub>mag</sub> were determined via the sequential extraction procedure of [Poulton and](#)  
216 [Canfield \(2005\)](#). Approximately 100 mg of sample powder was first subjected  
217 to a sodium acetate leach (buffered to pH = 4.5 with acetic acid) at 50 °C for 48  
218 hours for the extraction of Fe<sub>carb</sub>. The sample residue was then leached in  
219 sodium dithionite (50 g/L sodium dithionite, 58.82 g/l sodium citrate and 20 ml/l  
220 acetic acid) at room temperature for 2 hours, to extract Fe<sub>ox</sub>. Finally, the

221 remaining solid sample was treated with ammonium oxalate solution (0.2 M  
222 ammonium oxalate and 0.17 M oxalic acid) at room temperature for 6 hours, to  
223 extract  $Fe_{mag}$ . All extraction solutions were measured at the Beijing Research  
224 Institute of Uranium Geology by atomic absorption spectroscopy (AAS), with  
225 RSDs of <5% for Fe in all fractions.  $Fe_{py}$  was calculated from the pyrite sulfur  
226 extracted as an  $Ag_2S$  precipitate following the chromium reduction method  
227 ([Canfield et al., 1986](#)).

228 Organic carbon and nitrogen isotope ratios were measured using a Thermo  
229 Finnigan MAT 253 isotope ratio mass spectrometer interfaced to a Flash EA  
230 2000 elemental analyzer and a ConFlo IV continuous flow interface at the  
231 Beijing Research Institute of Uranium Geology. For organic carbon isotope  
232 measurements, 50 – 100 mg of sample was weighed and digested in 2 mol/L  
233 HCl to ensure complete carbonate removal. Residues were washed with  
234 distilled water to remove chlorides and dried at 70°C for 8 h. The decalcified  
235 sample powder was then weighed into tin capsules for organic carbon isotope  
236 measurements. Carbon isotope values ( $\delta^{13}C_{org}$ ) are reported in per mil relative  
237 to the international VPDB (Vienna Pee Dee Belemnite) standard. The  
238 analytical uncertainties were monitored by two international standards  
239 (USGS40,  $\delta^{13}C = -26.39\text{‰}$ ; IAEA-600,  $\delta^{13}C = -24.8\text{‰}$ ) and a China national  
240 standard (GSW04407,  $\delta^{13}C = -22.43\text{‰}$ ), with replicate analyses yielding a  
241 standard deviation of  $\pm 0.3\text{‰}$  for  $\delta^{13}C_{org}$ .

242 Samples for N isotope analysis were first analyzed for their total nitrogen

243 content (TN). Only those samples with TN >0.012 mg (>0.006%) were  
244 considered to provide reliable nitrogen isotope results (Wang et al., 2015).  
245 Approximately 30 – 150 mg of each bulk sample powder was weighed into a tin  
246 capsule and a carbon-absorbing trap was used in the EA to avoid interferences  
247 during the analysis due to the low N content and high C content of the marine  
248 shale samples. The nitrogen isotopic composition of sedimentary rocks  
249 ( $\delta^{15}\text{N}_{\text{sed}}$ ) is reported in per mil relative to atmospheric  $\text{N}_2$ . The analytical  
250 uncertainties were monitored by three international standards (USGS40,  $\delta^{15}\text{N}$   
251 =  $-4.52\text{‰}$ ; IAEA-600,  $\delta^{15}\text{N}$  =  $+1.0\text{‰}$ ; IAEA-N-2,  $\delta^{15}\text{N}$  =  $+20.3\text{‰}$ ) with replicate  
252 analyses yielding a standard deviation of  $\pm 0.4\text{‰}$  for  $\delta^{15}\text{N}$ .

253

## 254 4. Results

255 Nitrogen ( $\delta^{15}\text{N}_{\text{sed}}$ ) and organic carbon ( $\delta^{13}\text{C}_{\text{org}}$ ) isotopes, total organic  
256 carbon (TOC), total nitrogen (TN), Fe speciation, and redox-sensitive trace  
257 element (e.g. Mo, U, V) concentrations from the outer-shelf Zhongnancun  
258 section are presented in Table S1, and selected stratigraphic trends are  
259 illustrated in Fig. 2.

260 Three chert samples, eight black shale samples and one sulfide ore sample  
261 were analysed from Interval 1. The three chert samples contain relatively low  
262 TOC, TN and RSTE concentrations, ranging from 0.82 to 1.21 wt.% (mean =  
263 1.03 wt.%) for TOC, from 0.05 to 0.09 wt.% (mean = 0.07 wt.%) for TN, from  
264 4.1 to 4.8 ppm (mean = 4.5 ppm) for U, from 101 to 480 ppm (mean = 297 ppm)

265 for V, and from 6.8 to 18.5 ppm (mean = 12.2 ppm) for Mo. The  $Fe_T$   
266 concentrations for chert samples range from 0.68 to 0.76 wt.%, the  $Fe_{HR}/Fe_T$   
267 and  $Fe_{Py}/Fe_{HR}$  values range from 0.28 to 0.41 and 0.04 to 0.05, respectively.

268 The black shales from Interval 1 are characterized by higher TOC, TN and  
269 RSTE concentrations. The TOC values range from 4.27 to 12.08 wt. (mean =  
270 7.69 wt.%), TN values range from 0.09 to 0.16 wt.% (mean = 0.12 wt.%), U  
271 concentrations range from 23.8 to 112 ppm (mean = 40.0 ppm), V  
272 concentrations range from 1211 to 4872 ppm (mean = 2594 ppm), and Mo  
273 concentrations range from 74.3 to 208 ppm (mean = 119 ppm). The Mo/TOC  
274 ratios are between 8 and 21 (mean = 17). The sulfide ore sample preserves  
275 high TOC (10.72 wt.%), TN (0.12 wt.%) and RSTE concentrations (41850 ppm  
276 for Mo, 612 ppm for V, and 120 ppm for U), with a high Mo/TOC ratio (3904).  
277 The  $Fe_T$  concentrations for shale samples range from 1.76 to 11.50 wt.%, and  
278  $Fe_{HR}/Fe_T$  and  $Fe_{Py}/Fe_{HR}$  values for black shales range from 0.67 to 0.89 and  
279 0.66 to 0.85, respectively. The  $\delta^{13}C_{org}$  values in Interval 1 preserve a  
280 prominent negative excursion from -31.2‰ down to a nadir of -33.8‰. Values  
281 for  $\delta^{15}N_{sed}$  are between +1.2 to -0.6‰, with the exception of a prominent outlier  
282 at -4.2‰.

283 In comparison to Interval 1, black shale samples of Interval 2 generally  
284 preserve lower TOC (with the exception of two samples at the bottom of this  
285 interval), TN and RSTE concentrations. Total organic carbon concentrations  
286 are in the range 3.14 to 15.56 wt.% (mean = 5.39 wt.%), and TN ranges from

287 0.06 to 0.13 wt.% (mean = 0.09 wt.%). The concentration of U is in the range  
288 19.2 to 68.6 ppm (average = 29.9 ppm), V ranges from 362 ppm to 1453 ppm  
289 (mean = 972 ppm), Mo ranges from 7.3 ppm to 125 ppm (mean = 41.1 ppm),  
290 and Mo/TOC is in the range 2 to 15 ppm/wt% (mean = 7 ppm/wt%). The Fe<sub>T</sub>  
291 concentrations range from 0.78 to 2.32 wt.%, and Fe<sub>HR</sub>/Fe<sub>T</sub> and Fe<sub>Py</sub>/Fe<sub>HR</sub>  
292 ratios range from 0.38 to 0.88 and 0.01 to 0.72, respectively. Values for δ<sup>13</sup>C<sub>org</sub>  
293 initially increase following the negative excursion exhibited in Interval 1, from  
294 -32.1 to -29.6‰, before decreasing once more to -31.4‰ near the top of  
295 Interval 2. Values for δ<sup>15</sup>N<sub>sed</sub> vary between +0.6 and +2.7‰, and exhibit an  
296 overall positive excursion in this interval.

297 Silty black shales of Interval 3 preserve the lowest TOC, TN and RSTE  
298 concentrations of the three intervals. The TOC concentrations range from 1.32  
299 to 2.73 wt.% (mean = 1.98 wt.%), and TN values range from 0.06 to 0.11 wt.%  
300 (mean = 0.09 wt.%). The concentration of U is in the range 15.2 to 27.3 ppm  
301 (mean = 19.0 ppm), V ranges from 252 to 856 ppm (mean = 446 ppm), Mo  
302 ranges from 4.5 to 14.8 ppm (mean = 8.6 ppm), and the Mo/TOC ratio is in the  
303 range 3 – 6 ppm/wt% (mean = 4 ppm/wt%). The Fe<sub>T</sub> concentrations range  
304 from 1.25 to 2.46 wt.%, and Fe<sub>HR</sub>/Fe<sub>T</sub> and Fe<sub>Py</sub>/Fe<sub>HR</sub> values range from 0.21 to  
305 0.48 and 0.11 to 0.42, respectively. Values for δ<sup>13</sup>C<sub>org</sub> in Interval 3 are  
306 relatively invariant, and range from -30.5 to -30.0‰, whilst δ<sup>15</sup>N<sub>sed</sub> decreases  
307 from +1.1 to +0.2‰.

308

## 5. Discussion

### 5.1. Palaeoredox evolution of the early Cambrian Nanhua Basin

The ratio  $Fe_{HR}/Fe_T$ , together with the extent of sulfidation of the highly reactive iron pool ( $Fe_{Py}/Fe_{HR}$ ), can provide valuable information about local bottom water redox conditions (e.g. [Poulton et al., 2004](#); [Canfield et al., 2008](#); [Poulton and Canfield, 2011](#)). Generally,  $Fe_{HR}/Fe_T$  ratios  $> 0.38$  suggest anoxic water column conditions, with ratios  $< 0.22$  providing strong support for oxic depositional conditions ([Raiswell and Canfield, 1998](#); [Raiswell et al., 2001](#); [Poulton and Raiswell, 2002](#); [Poulton and Canfield, 2011](#)). Enrichments in  $Fe_{HR}$  (i.e.  $Fe_{HR}/Fe_T > 0.38$ ) commonly occur under anoxic conditions due to water column precipitation of either Fe sulfide minerals (in euxinic settings) or non-sulfidized Fe minerals (in anoxic ferruginous settings) ([Canfield et al., 1996](#); [Raiswell and Canfield, 1998](#); [Poulton et al., 2004](#); [Poulton and Canfield, 2011](#)).  $Fe_{HR}/Fe_T$  ratios between 0.22 – 0.38 are considered equivocal due to the potential dilution of  $Fe_{HR}$  enrichments either as a consequence of rapid sedimentation or post-depositional transfer of unsulphidized  $Fe_{HR}$  to Fe-rich clay minerals during early diagenesis (e.g. [Poulton and Raiswell, 2002](#); [Poulton et al., 2010](#)). In such cases, additional insight into depositional redox conditions may be gained from Fe/Al ratios and RSTE systematics (e.g. [Doyle et al., 2018](#)). For sediments deposited under anoxic water column conditions,  $Fe_{Py}/Fe_{HR}$  ratios of  $< 0.7$  and  $> 0.7-0.8$  are commonly used to distinguish between ferruginous and euxinic conditions, respectively (e.g.

331 [Poulton et al., 2004](#); [Poulton and Canfield, 2011](#); [Raiswell and Canfield,](#)  
332 [2012](#)). It is necessary to carefully consider the lithology when applying Fe  
333 based redox proxies ([Raiswell et al. 2018](#)). For lithologies where clastic input  
334 has been diluted (e.g. carbonates, cherts) threshold values for total iron and  
335 organic carbon (> 0.5% for both) have been proposed as minimum  
336 requirements for using the iron-based redox proxies (e.g. [Clarkson et al.,](#)  
337 [2014](#); [Raiswell et al. 2018](#)). The  $Fe_T$  and TOC concentrations in all samples  
338 from this study are greater than 0.5%, indicating that the iron speciation proxy  
339 is a valid approach for reconstructing depositional paleoredox conditions.

340 At the Zhongnancun section, black shale samples from Interval 1 have  
341 elevated  $Fe_{HR}/Fe_T$  (0.67-0.89), with generally high  $Fe_{Py}/Fe_{HR}$  (0.66-0.85),  
342 which is consistent with anoxic water column conditions, and at least  
343 intermittent euxinia. Elevated  $Fe_{HR}/Fe_T$  and a decrease in  $Fe_{Py}/Fe_{HR}$  supports  
344 a shift to dominantly ferruginous conditions up-section into Interval 2 ([Fig. 2](#)).  
345 Samples from Interval 3 have  $Fe_{HR}/Fe_T$  ratios that fall in the equivocal zone  
346 (except for one sample at 33.4 m, where  $Fe_{HR}/Fe_T = 0.48$ ), and we thus utilize  
347 RSTE systematics to provide additional insight into water column redox  
348 conditions during deposition of these samples.

349 The degree to which Mo, U and V are enriched in organic-rich mudstones  
350 (ORMs), alongside co-variation in total organic carbon (TOC), can be  
351 effectively used to track both depositional paleoredox conditions and the size  
352 of seawater trace metal reservoirs ([Algeo and Lyons, 2006](#); [Anbar et al., 2007](#);

353 [Scott et al., 2008](#); [Sahoo et al., 2012](#)). Starting with samples from Interval 1  
354 ([Fig. 2](#)), the high level of Mo enrichment (mean for black shale samples = 119  
355 ppm) is consistent with the presented Fe speciation data, and suggests  
356 dominantly euxinic conditions (e.g. [Scott and Lyons, 2012](#)). However, the  
357 co-variation between Mo and TOC is not particularly strong ( $R^2 = 0.41$ ; [Fig.](#)  
358 [3a](#)), which might be consistent with variable water column H<sub>2</sub>S concentrations,  
359 since persistently high H<sub>2</sub>S is required to effectively draw down Mo  
360 ([Tribovillard et al., 2006](#)). Indeed, variability in H<sub>2</sub>S concentrations would be  
361 consistent with our Fe speciation data, whereby some of the Fe<sub>Py</sub>/Fe<sub>HR</sub> ratios  
362 fall slightly below the 0.7 threshold for robust identification of water column  
363 euxinia, implying more limited sulfide availability. As with Mo, however,  
364 enrichments in V (612 to 4872 ppm, average 2373 ppm) for ORMs from  
365 Interval 1 ([Fig. 2](#)) are consistent with generally euxinic water column  
366 conditions ([Tribovillard et al., 2006](#)).

367 The Mo and TOC enrichments in Interval 2 remain high, but are lower than  
368 those of Interval 1 ([Fig. 2](#)), consistent with the interpretation of anoxic  
369 ferruginous conditions from Fe speciation data. Uranium is not commonly  
370 enriched under oxic/dysoxic conditions, but is instead present primarily as  
371 carbonate complexes that are chemically unreactive (see references in [Algeo](#)  
372 [and Tribovillard, 2009](#)). Strong U enrichment does, however, occur under  
373 anoxic conditions, where enrichments commonly show a positive correlation  
374 with TOC ([Fig. 3b](#); [Algeo and Tribovillard, 2009](#)). By contrast, the positive

375 correlation ( $R^2 = 0.66$ ) between Mo and TOC, together with relatively low Mo  
376 concentrations ( $9 \pm 5$  ppm; [Fig. 3a](#)), provides evidence that Mo was  
377 sequestered in association with organic matter in an oxic or dysoxic  
378 environment during deposition of Interval 3 ([Scott et al., 2008](#)), which  
379 suggests that the  $Fe_{HR}/Fe_T$  ratios of  $<0.38$  ([Fig. 2](#)) are indeed recording  
380 oxic/dysoxic water column conditions.

381 Co-variation between Mo and U in marine basins can provide an additional  
382 level of interpretation concerning trace element enrichment mechanisms and  
383 possible water mass restriction (e.g. [Tribovillard et al., 2006](#); [Algeo and](#)  
384 [Tribovillard, 2009](#)). Molybdenum and U enrichment factors from the  
385 Zhongnancun section are largely consistent with the pattern observed in the  
386 modern open ocean ([Fig. 4](#)). Samples from Interval 1 exhibit high  $Mo_{EF}$ ,  $U_{EF}$   
387 and Mo/U ratios, which support sedimentary enrichment of Mo and U from a  
388 dominantly euxinic water column. Samples from Interval 2 preserve lower  
389 concentrations of Mo and U, and some samples have elevated Mo/U ratios  
390 relative to the modern open ocean trend, which may suggest a weak  
391 particulate shuttle ([Algeo and Tribovillard, 2009](#)). The preferential  
392 complexation of Mo with Fe-Mn oxyhydroxides can lead to the enhanced  
393 transfer of Mo into sediments, thereby resulting in elevated Mo/U ratios  
394 ([Algeo and Tribovillard, 2009](#)). This particulate shuttle effect is most  
395 pronounced where the oxic – anoxic chemocline is located close to the  
396 sediment water interface (e.g. modern Baltic Sea, [Scholz et al., 2013](#)).

397 The relative importance of the particulate shuttle for Mo enrichment can be  
398 assessed from  $Mo_{EF}$  and  $U_{EF}$  data compiled for multiple lower Cambrian  
399 sections (Fig. 4). The lowest  $Mo_{EF}$ ,  $U_{EF}$  and Mo/U ratios are found in samples  
400 from Interval 3, supporting oxic/suboxic conditions. However, it is worth noting  
401 that the Mo enrichment associated with the Fe-Mn oxyhydroxide particulate  
402 shuttle may also complicate the interpretation of Mo and TOC co-variation  
403 (Magnall et al. 2018), and may be an alternative explanation for the lack of  
404 correlation between Mo and TOC in Intervals 1 and 2.

405 The redox constraints from the Zhongnancun section can be compared to  
406 other studies conducted on correlative sections (e.g. Jin et al., 2016) from the  
407 Yangtze Block (Fig. 5; Table S2). Euxinic conditions prevailed in the  
408 transitional zone between oxic waters on the platform and dominantly  
409 ferruginous deeper waters on the slope/basin during Cambrian Stage 2.  
410 Subsequently, euxinic conditions were progressively replaced by anoxic,  
411 non-sulfidic water column conditions as the sea level regression proceeded  
412 (early-middle Cambrian Stage 3). Oxic conditions were progressively  
413 established in shelf settings during late Cambrian Stage 3 with anoxia largely  
414 maintained in slope and basin environments and euxinic conditions in deeper  
415 water environments.

416 These observations are consistent with a stratified ocean model in which  
417 euxinic mid-depth waters were dynamically maintained between oxic surface  
418 waters and ferruginous deeper waters. Progressive ventilation, first of shallow,

419 and then shelf and slope environments, proceeded during Cambrian Stage 2  
420 to 3 (e.g. [Jin et al., 2016](#); [Li et al., 2017](#)). By early Cambrian Stage 4 (~514  
421 Ma), oxic conditions may have been established in shallow shelf (i.e. Jinsha  
422 section) and slope settings, and in deeper waters (i.e. Longbizui section),  
423 while mid-depth environments (i.e. Wengan and Songtao sections) remained  
424 anoxic ([Fig. 5](#)), suggesting a redox structure similar to an oxygen minimum  
425 zone (OMZ). In terms of the broader redox landscape, geochemical proxies  
426 that are sensitive to long term terrestrial weathering processes provide  
427 evidence that global tectonic activity during the Ediacaran-Cambrian could  
428 have resulted in the increased supply of nutrients to the oceans, primary  
429 productivity and associated photosynthetic O<sub>2</sub> release ([Campbell and Squire,](#)  
430 [2010](#)). Yet it remains an ongoing challenge to differentiate between local,  
431 regional, and global scale controls on the spatio-temporal redox evolution of  
432 ancient marine systems. In the case of the Yangtze Ocean, for example, a  
433 marine regression during Cambrian Stage 3 could have simply resulted in the  
434 offshore migration of euxinic waters (e.g. [Bowyer et al. 2017](#)). In the following,  
435 we evaluate N isotope data from the Zhongnancun section together with  
436 compiled data from the literature to further evaluate the redox architecture of  
437 the Cambrian Yangtze Ocean.

438

## 439 **5.2. Nitrogen cycling in the early Cambrian Yangtze ocean**

440 The isotopic composition of nitrogen ( $\delta^{15}\text{N}$  values) can provide additional

441 information for studies on seawater paleoredox (Fig. 6). In the modern  
442 oceans, the primary source of bioavailable nitrogen to the marine system is  
443 via fixation of atmospheric  $N_2$  ( $N_2$ -fixation), which transforms molecular  $N_2$   
444 into organic matter (via  $NH_4^+$ ) through ammonification. There is negligible  
445 isotopic fractionation associated with ammonification ( $-1\text{‰}$  on average),  
446 however under  $Fe^{2+}$ -rich or thermophilic conditions, fractionation may be as  
447 large as  $-4\text{‰}$  (e.g. Zerkle et al., 2008; Zhang et al., 2014). In oxic  
448 environments, the  $NH_4^+$  released by breakdown of organic matter is rapidly  
449 oxidized to  $NO_2^-$  and then to  $NO_3^-$  through nitrification, also with negligible  
450 fractionation. Assimilation of  $NO_3^-$  results in isotopic fractionation with  $\epsilon_{org-NO_3}$   
451 between  $0\text{‰}$  and  $-10\text{‰}$  in  $NO_3^-$  limited and  $NO_3^-$  replete conditions,  
452 respectively (Pennock et al., 1996). In dysoxic to anoxic environments, the  
453 removal of nitrogen from the marine system ( $NO_3^-$ ,  $NH_4^+$  and  $NO_2^-$  are  
454 converted into gaseous species  $NO_2$  or  $N_2$ ) takes place via denitrification and  
455 anammox, with large fractionations of  $\sim 20\text{-}30\text{‰}$  in the water column, and  
456 negligible fractionation in the sediments (Sigman et al., 2009; Lam et al.,  
457 2009; Lam and Kuypers, 2011).

458 A recent compilation of published  $\delta^{15}N$  values from the Yangtze Block  
459 documented modern-like  $\delta^{15}N$  values during Cambrian Stage 3, implying that  
460 a large  $NO_3^-$  reservoir may have built up in well-oxygenated seawater during  
461 this time interval (Wang et al., 2018). Clearly, this is not consistent with the  
462 stratified ocean model suggested by the redox conditions documented across

463 the Yangtze Block (e.g. [Jin et al., 2016](#); [Li et al., 2017](#)). In order to better  
464 understand the prevailing redox structure and operation of the N cycle in the  
465 early Cambrian Yangtze ocean, we coupled inorganic redox proxies with  $\delta^{15}\text{N}$   
466 data from multiple sections across the Yangtze Block, as well as sections  
467 from the uplift margin close to the Cathaysia Block ([Fig. 7](#); [Table S3](#)).

### 468 *5.2.1 Late Cambrian Stage 2*

469 During late Cambrian Stage 2, the majority of deep water sections  
470 (slope-basin) across the Yangtze Block show  $\delta^{15}\text{N}$  values that range from -2  
471 to 2‰ ([Fig. 7](#)), with a mean value close to the nitrogen isotopic composition of  
472 the atmosphere (0‰). Isotopic variability within this range can be explained  
473 by three possible mechanisms (see [Stüeken, 2013](#) for detailed discussion): (i)  
474 Nitrogen fixation as the dominant pathway for nitrogen cycling, especially  
475 under anoxic conditions where nitrification (strictly dependent on  $\text{O}_2$ ) is  
476 inhibited. Biological nitrogen fixation (reduction of  $\text{N}_2$  to  $\text{NH}_4^+$ ) with the most  
477 common Mo-based nitrogenase enzyme imparts a minimal isotopic  
478 fractionation of  $-1\text{‰}$  on average, with a range from  $-2$  to  $+1\text{‰}$  ([Zhang et al.,](#)  
479 [2014](#); [Stüeken et al., 2016](#)). This scenario is likely in the case of the Yangtze  
480 ocean during the late Cambrian Stage 2, because iron speciation data  
481 indicates that seawater was dominantly anoxic at depth ([Fig. 5](#)) and the  
482 sediments in this interval are characterized by high Mo concentrations ([Scott](#)  
483 [et al., 2008](#); [Chen et al., 2015](#)). (ii) Fixed nitrogen is rapidly nitrified and then  
484 quantitatively denitrified due to the redox gradient in the water column.

485 Scenario (ii) is a possible explanation for the N isotope signals preserved at  
486 the shallowest water Xiaotan section, since intermittent oxic conditions  
487 occurred in the late Cambrian Stage 2. (iii) Under oxic conditions, fixed  
488 nitrogen is readily nitrified and denitrification is restricted to sediments.  
489 Scenario (iii) is unlikely because widespread anoxia has been well  
490 documented in this stage (e.g. [Feng et al., 2014](#); [Wang et al., 2015](#); [Jin et al.,](#)  
491 [2016](#); [Fig. 5](#)). Thus, the biogeochemical pathway of the nitrogen cycle in the  
492 deep water during the late Cambrian Stage 2 was likely dominated by N<sub>2</sub>  
493 fixation ([Fig. 8a](#)).

494 Anomalous negative  $\delta^{15}\text{N}$  values ( $< -2\text{‰}$ ) are preserved in some samples  
495 from the outer-shelf Zhongnancun ([Fig. 2](#)) and Sancha sections, and also  
496 from the base of the inner-shelf CJ2 section ([Fig. 7](#)). Two alternative  
497 mechanisms can be considered to explain these negative  $\delta^{15}\text{N}$  values: (i) N<sub>2</sub>  
498 fixation using alternative nitrogenases containing V or Fe as cofactors  
499 (instead of the more common Mo) can produce large isotopic fractionations of  
500 -6 to -8‰ ([Zhang et al., 2014](#)); (ii) non-quantitative NH<sub>4</sub><sup>+</sup> assimilation by  
501 organisms in NH<sub>4</sub><sup>+</sup> replete conditions could produce large fractionations of -4  
502 to -27‰, depending on NH<sub>4</sub><sup>+</sup> concentrations ([Pennock et al., 1996](#)).

503 Scenario (i) has been invoked to explain the  $\delta^{15}\text{N}$  values (-2 to -4‰)  
504 preserved in Cretaceous Oceanic Anoxic Event 2 (OAE-2) black shales, due  
505 to Mo-limited ocean anoxia ([Zhang et al., 2014](#)). However, this scenario  
506 seems unlikely, since even in the Mo-depleted, Fe-rich Precambrian oceans

507 there is thus far no convincing evidence of biological N<sub>2</sub> fixation with V or Fe  
508 nitrogenases (Stüeken et al., 2013). Furthermore, this interpretation is also  
509 inconsistent with the high Mo concentration recorded in sediments during this  
510 period (Wang et al., 2015; Hammarlund et al., 2017; Scott et al., 2008; Chen  
511 et al., 2015). Scenario (ii) has been invoked to explain the negative  $\delta^{15}\text{N}$   
512 values (as low as -4‰) during Cretaceous OAE-2 (Higgins et al., 2012) and  
513 similar  $\delta^{15}\text{N}$  values (as low as -4.7‰) in the late Paleoproterozoic (Papineau  
514 et al., 2009). This mechanism would be a reasonable interpretation for the  
515 low  $\delta^{15}\text{N}$  values in this study (Fig. 8a), because the negative  $\delta^{15}\text{N}$  values  
516 observed in shelf sections correspond well with euxinia (Fig. 7). Under euxinic  
517 conditions, the organic-bound NH<sub>4</sub><sup>+</sup> is likely to accumulate to high  
518 concentrations in the water column (review by Stüeken et al., 2016 for  
519 details).

520 Previous studies have suggested that partial NH<sub>4</sub><sup>+</sup> assimilation by  
521 anaerobic bacteria (e.g. green or purple sulfur bacteria) could result in these  
522 low  $\delta^{15}\text{N}$  values in the early Cambrian Yangtze ocean during Cambrian Stage  
523 2 (Wang et al., 2018). The NH<sub>4</sub><sup>+</sup> replete conditions may have built up in the  
524 shelf area due to strong upwelling of NH<sub>4</sub><sup>+</sup>-rich anoxic waters from the deep  
525 ocean. These results are further consistent with a shallow chemocline and  
526 photic zone euxinia during the late Cambrian Stage 2. The majority of  
527 samples from shelf sections, however, preserve  $\delta^{15}\text{N}$  values typical of  
528 nitrogen fixation (from -2 to 2‰), which may be attributable to the NH<sub>4</sub><sup>+</sup>

529 transported from deep water being consumed quantitatively and thereby  
530 masking the fractionation associated with  $\text{NH}_4^+$  assimilation.

### 531 *5.2.2 Cambrian Stage 3*

532 During the early-middle Cambrian Stage 3, widespread anoxic conditions  
533 existed in the Yangtze ocean (Figs 5 and 7). However, distinctive  $\delta^{15}\text{N}$  values  
534 are preserved in different settings, with more positive values (generally  
535 between 0 and 3‰) recorded in the shelf environment and lower values (from  
536 -2 to 2‰) recorded in slope-basin settings (Figs. 7 and 9).

537 The positive shift in  $\delta^{15}\text{N}$  values observed in sections from the inner-shelf  
538 and outer-shelf can be explained by three possible scenarios (Stüeken, 2013;  
539 Ader et al., 2016; Stüeken et al., 2016; Koehler et al., 2017): (i) Partial  
540 assimilation of  $\text{NH}_4^+$  would preferentially consume isotopically light nitrogen  
541 and leave the residual  $\text{NH}_4^+$  pool enriched in  $^{15}\text{N}$  (Papineau et al., 2009); (ii)  
542 Partial nitrification of  $\text{NH}_4^+$  can produce an isotopically light nitrate pool while  
543 leaving a residual  $\text{NH}_4^+$  pool enriched in  $^{15}\text{N}$ , because nitrification prefers  
544 lighter isotopes (Thomazo et al., 2011). Scenarios (i) and (ii) are unlikely  
545 explanations for the positive  $\delta^{15}\text{N}$  shift in the shelf area of the early Cambrian  
546 Yangtze ocean for the following reasons. Firstly, mechanism (i) would result in  
547 two distinct isotopic facies, one which preserves low  $\delta^{15}\text{N}$  values (<-2‰) and  
548 one which preserves high  $\delta^{15}\text{N}$  values (>1‰). However, samples from the  
549 inner-shelf to the basin during this period do not record very negative  $\delta^{15}\text{N}$   
550 values. For example, the lowest  $\delta^{15}\text{N}$  value from the slope (Longbizui) section

551 is -2‰ and most values from deep water sections are close to 0‰, consistent  
552 with N<sub>2</sub> fixation (-2 to +2‰, [Stüeken, 2013](#)). Regarding scenario (ii), partial  
553 nitrification has so far been considered to occur only in marine environments  
554 that undergo transient seasonal changes, with no evidence for this process  
555 occurring over longer geologic timescales ([Hadas et al., 2009](#); [Granger et al.,](#)  
556 [2011](#)). This leaves scenario (iii), whereby partial denitrification in the water  
557 column leaves the residual nitrate pool enriched in <sup>15</sup>N, because denitrification  
558 produces isotopically light nitrogenous gases, which removes <sup>14</sup>N from the  
559 system (e.g. [Cline and Kaplan, 1975](#)). Scenario (iii) is most likely in the case of  
560 the early Cambrian Yangtze ocean and nitrate appears to have been more  
561 abundant in shelf environment ([Fig. 8b](#)). This has also been considered as the  
562 main mechanism for the production of positive δ<sup>15</sup>N values in the modern  
563 ocean (e.g. [Lam et al., 2009](#); [Tesdal et al., 2013](#)) as well as in the early  
564 Cambrian Yangtze ocean ([Hammarlund et al., 2017](#); [Wang et al., 2018](#)). These  
565 positive δ<sup>15</sup>N excursion intervals have a good correspondence with ferruginous  
566 conditions, suggesting that the water column may also have experienced  
567 nitrogenous conditions. Oxygen is required for nitrification of ammonium to  
568 nitrate ([Koehler et al., 2017](#)), thereby higher nitrate levels in the shelf area  
569 suggest that oxic-suboxic conditions may have been established in shelf  
570 environment.

571 The δ<sup>15</sup>N values (-2 to +2‰) of slope – basin sections during this period are  
572 similar to those in the late Cambrian Stage 2. The invariability of δ<sup>15</sup>N values in

573 these sections is consistent with the maintenance of anoxic and ferruginous  
574 conditions in deeper waters throughout Cambrian Stage 2 – 3 (Jin et al., 2016;  
575 Li et al., 2017), reflecting nitrogen limitation in slope – basin parts of the early  
576 Cambrian Yangtze ocean (Fig. 8b). However, the positive  $\delta^{15}\text{N}$  excursions are  
577 found in the sections (Yanjia section, Chunye 1 drill core and Silikou section)  
578 close to the Cathaysia Block, and are interpreted to have resulted from  
579 denitrification (Wang et al., 2018; Zhang et al., 2018). These sections were  
580 considered to represent a deep water environment (Wang et al., 2018).  
581 Previous studies have suggested that at least the western Zhejiang area  
582 (where the Yanjia section and Chunye 1 drill core were located) was a  
583 semi-restricted gulf environment (Xue and Yu, 1979; Huang and Zhang, 1988;  
584 Xiang et al., 2018), and thus the nitrogen cycle here may have been different to  
585 that of the open ocean.

586 The  $\delta^{15}\text{N}$  values preserved in all sections (Fig. 10) are, however, lower than  
587 the isotopic composition of modern oceanic sediments (+5‰, Tesdal et al.,  
588 2013). Lower  $\delta^{15}\text{N}$  values documented in these sections can be explained by  
589 low oceanic dissolved oxygen and nitrate concentrations (Stüeken, 2013;  
590 Koehler et al., 2017). A small nitrate reservoir and low oxygen concentration in  
591 the water column would have decreased the nitrate inventory of the ocean  
592 without significantly increasing residual nitrate  $\delta^{15}\text{N}$  values, thereby allowing  
593 preservation of a N isotopic signature characteristic of  $\text{N}_2$  fixation (Stüeken,  
594 2013; Ader et al., 2016; Kipp et al., 2018). It is noteworthy that the redox

595 differences and latitude variations should also be taken into account when  
596 comparing ancient and modern oceans (e.g. [Koehler et al., 2019](#)). The  $\delta^{15}\text{N}$   
597 excursions observed in each of the shelf sections are of a similar magnitude  
598 ( $\sim 3\text{‰}$ ), which may imply that the  $\delta^{15}\text{N}$  values in these sections could have  
599 recorded the values of the regional nitrate reservoir during the early Cambrian  
600 period, which was lower than that of the modern ocean. Although data from  
601 Yangtze basin cannot capture global trends in marine nitrogen cycling during  
602 early Cambrian and more data outside South China await further analysis and  
603 study here and elsewhere, it is possible that they may in part reflect a global  
604 phenomenon. This explanation is supported by long-term secular variation in  
605 the marine nitrogen cycle, suggesting that  $^{15}\text{N}$ -depleted isotopic compositions  
606 in the Cambrian ocean were likely due to enhanced sedimentary denitrification,  
607 without significant nitrogen isotopic fractionation effects during greenhouse  
608 highstands ([Algeo et al., 2014](#)). Taken together, we conclude that the  
609 spatiotemporal distribution of  $\delta^{15}\text{N}$  values, and the gradients in C and N  
610 isotopes ([Fig. 9](#)), suggest a stratified redox structure, consistent with that  
611 recorded by iron speciation and RSTE data.

612

### 613 **5.3. Biological implications**

614 During the late Cambrian Stage 2 to earliest Stage 3, continental margin  
615 environments such as the Yangtze Block, South China, exhibited variable  
616 degrees of anoxia and palaeoredox stratification. In such environments,

617 negative carbonate carbon isotope excursions and low  $\delta^{15}\text{N}$  values have been  
618 suggested to indicate periodic shoaling of the redoxcline into the photic zone  
619 (e.g. [Wang et al., 2018](#); [Chen et al., 2019](#)). The extensive anoxia and  
620 intermittent photic zone euxinia, as confirmed by iron speciation and RSTE  
621 data, may have resulted in the extinction of small shelly fossils in early  
622 Cambrian oceans ([Zhu et al., 2007](#); [Wang et al., 2018](#)).

623 The  $\delta^{15}\text{N}$  gradient in the early Cambrian Yangtze ocean during early –  
624 middle Stage 3 ([Fig. 9](#)) is similar to the Mesoproterozoic Belt Supergroup (~  
625 1.4 billion years ago, Ga; [Stüeken, 2013](#)), and the Bangemall (~ 1.5 Ga) and  
626 Roper (~ 1.4 – 1.5 Ga) basins ([Koehler et al., 2017](#)), suggesting that the early  
627 Cambrian Yangtze ocean was characterized by generally low nitrate  
628 concentrations with a minimum in offshore deep water environments. It has  
629 been hypothesized that nitrogen availability may have played an important role  
630 in the evolutionary innovation of eukaryotes ([Anbar and Knoll, 2002](#)). If correct,  
631 the nitrate gradient may have restricted large-celled eukaryotes to near-shore  
632 environments, as in the case of the early evolution of eukaryotes in the  
633 Mesoproterozoic oceans ([Stüeken, 2013](#); [Koehler et al., 2017](#)). The nitrate  
634 gradient observed in this study can be linked to fossil distributions in the early  
635 Cambrian Yangtze ocean, as demonstrated by [Jin et al. \(2016\)](#). These authors  
636 showed that the complexity of early animal ecosystems is spatially  
637 heterogeneous, with increased complexity in near-shore environments  
638 containing higher oxygen levels ([Figs 5 and 7](#)). The increased nitrogen

639 availability in shelf environments may have enhanced the biological pump and  
640 the evolution of large-celled eukaryotic phytoplankton (Brocks et al., 2017;  
641 Wang et al., 2018). A corresponding increase in the size of organic particulates  
642 and faster sinking rates may have enhanced organic matter burial, thus  
643 reducing O<sub>2</sub> consumption in the water column and resulting in a positive  
644 feedback on further ocean oxygenation, and synchronized early animal  
645 radiations (Butterfield, 2009; Lenton et al., 2014).

646 Recently, He et al. (2019) documented a strong positive co-variation  
647 between carbonate  $\delta^{13}\text{C}$  values and carbonate-associated sulfate  $\delta^{34}\text{S}$  values  
648 in early Cambrian Siberian platform carbonates. The authors argued that this  
649 covariation records variability in atmospheric O<sub>2</sub> concentrations. Moreover,  
650 they suggest that episodic maxima in the biodiversity of animal phyla directly  
651 coincided with the extent of shallow-ocean oxygenation. Hammarlund et al.  
652 (2017) have shown that OMZ-type conditions persisted well into the interval  
653 characterized by the Chengjiang biota. However, the shallow shelf may have  
654 been dominantly well oxygenated at this time, providing a stable, oxygenated  
655 environment within which these energetically costly, motile lifestyles could  
656 have thrived.

657 When predatory animals, which produce larger fecal particulates, dominate  
658 the shallow water ecosystem, the sinking and burial of organic carbon is  
659 accelerated, thus reducing oxygen consumption in the water column and  
660 allowing oxygen to reach deeper waters (Logan et al., 1995). Furthermore,

661 sponges, which dominate the deep water ecosystem of the early Cambrian  
662 Yangtze ocean (Zhu, 2010; Fig. 5), may have also played a role in the  
663 accumulation of oxygen in the deep waters by filtering the reduced carbon in  
664 the water column (Lenton et al., 2014). The appearance of macrozooplankton  
665 (i.e. bivalved arthropod *Isoxys*) and suspension-feeding mesozooplankton (i.e.  
666 anomalocarid *Tamisiocaris borealis*) in Cambrian Stage 3 (Luo et al., 1994;  
667 Vinther et al., 2014) provides reliable paleontological evidence for this  
668 hypothesis. Although global Fe speciation data suggest that deep waters  
669 remained largely anoxic in some basins during Cambrian Stage 3 (Sperling et  
670 al., 2015; Li et al., 2017), oxic conditions (Fig. 5), and a transition from  
671 abundant sponge spicules to articulated sponges (Wang et al., 2012; Jin et al.,  
672 2016) observed at the deep water Longbizui section, may provide evidence for  
673 at least local ventilation of deep water settings (slope-basin) during Cambrian  
674 Stage 4 in South China. Furthermore, OMZ-type stratification with at least  
675 weakly oxygenated deeper waters has recently been recorded from detailed  
676 regional paleoredox assessments of lower Cambrian sediments of the Baltic  
677 Basin (Guilbaud et al., 2018), and South China (Hammarlund et al., 2017)  
678 raising the possibility for widespread restructuring of the paleoredox landscape  
679 by Cambrian Stage 4.

680

## 681 **6. Conclusions**

682 Multi-proxy geochemical data are reported for the outer-shelf Zhongnancun

683 section of the early Cambrian Yangtze Block in South China. Results reveal  
684 that the redox conditions progressively evolved from euxinic, through  
685 ferruginous, to oxic during deposition of the Niutitang Formation. Our new data  
686 combined with existing data from the shelf to the basin environment, suggest  
687 that during Cambrian stages 2 – 3, the Yangtze ocean was redox stratified with  
688 euxinic mid-depths dynamically maintained between oxic surface waters and  
689 ferruginous deeper waters. However, by early Cambrian Stage 4 (~514 Ma),  
690 deep waters may have become intermittently oxygenated.

691 Nitrogen isotope data from successions across the Yangtze Block show that,  
692 during late Cambrian Stage 2, N<sub>2</sub> fixation was the dominant biogeochemical  
693 pathway of the nitrogen cycle. Anomalously light  $\delta^{15}\text{N}$  values (<-2‰) observed  
694 in shelf sections correspond well with euxinia, suggesting that partial  
695 assimilation of NH<sub>4</sub><sup>+</sup> was the dominant pathway for nitrogen cycling in euxinic  
696 waters, and NH<sub>4</sub><sup>+</sup> may have built up to high concentrations.

697 During early – middle Cambrian Stage 3, a distinct gradient in  $\delta^{15}\text{N}$  is  
698 observed in the early Cambrian Yangtze ocean, with more positive values  
699 (between 0 and 3‰) recorded in shelf sections and lighter values (from -2 to  
700 2‰) recorded in slope-basin sections. The positive shift in  $\delta^{15}\text{N}$  values  
701 preserved in the shelf sections likely results from partial denitrification in the  
702 water column, while  $\delta^{15}\text{N}$  values of ~0‰, recorded in deeper water sections  
703 may have resulted from N<sub>2</sub> fixation. The  $\delta^{15}\text{N}$  values preserved in all sections  
704 are lower than those of the modern ocean, indicating that the early Cambrian

705 Yangtze ocean may be characterized by low nitrate concentrations.  
706 Furthermore, the spatiotemporal distribution of the  $\delta^{15}\text{N}$  values, together with  
707 the stratigraphic gradients in C and N isotopes, and Fe speciation data, are all  
708 consistent with a model of, at least, regional-scale palaeo-marine redox  
709 stratification.

710 The  $\delta^{15}\text{N}$  gradient in the early Cambrian Yangtze ocean is similar to that  
711 suggested for Mesoproterozoic oceans (Stüeken, 2013; Koehler et al., 2017),  
712 implying that nitrate was limited in offshore environments, restricting  
713 eukaryotes to near-shore environments. Increased nitrogen availability in shelf  
714 environments would have enhanced the biological pump and the evolution of  
715 large-celled eukaryotic phytoplankton, which may have produced a positive  
716 feedback on further ocean oxygenation, allowing for increased complexity and  
717 diversity of early animal ecosystems on oxic shelves.

718

## 719 **Acknowledgments**

720 This work was supported by the National Science and Technology Major  
721 Project (Grant No. 2016ZX05034-002-001), National Natural Science  
722 Foundation of China (Grant No. 41927801), Fundamental Research Funds  
723 for the Central Universities (Grant No. 2652019098), the  
724 Helmholtz-Rekrutierungsinitiative (SG and JM), SWP and FTB were funded by  
725 NERC (NE/R010129/1), and SWP acknowledges support from a Royal

726 Society Wolfson Research Merit Award. We thank the editor in chief Michael  
727 E. Böttcher and two reviewers (Eva E. Stüeken and Matthew C. Koehler) for  
728 their comments that significantly improved this paper.

729

## 730 **References**

731 Ader, M., Thomazo, C., Sansjofre, P., Busigny, V., Papineau, D., Laffont, R.,  
732 Cartigny, P., Halverson, G.P., 2016. Interpretation of the nitrogen isotopic  
733 composition of Precambrian sedimentary rocks: assumptions and  
734 perspectives. *Chem. Geol.* 429, 93-110.

735 Algeo, T., Rowe, H., Hower, J.C., Schwark, L., Herrmann, A., Heckel, P., 2008.  
736 Changes in ocean denitrification during Late Carboniferous  
737 glacial–interglacial cycles. *Nat. Geosci.* 1, 709-714.

738 Algeo, T.J., Lyons, T.W., 2006. Mo-total organic carbon covariation in modern  
739 anoxic marine environments: implications for analysis of paleoredox and  
740 paleohydrographic conditions. *Paleoceanography* 21, PA1016.

741 Algeo, T.J., Meyers, P.A., Robinson, R.S., Rowe, H., Jiang, G.Q., 2014.  
742 Icehouse-greenhouse variations in marine denitrification.  
743 *Biogeosciences* 11, 1273-1295.

744 Algeo, T.J., Rowe, H., 2012. Paleoceanographic applications of trace-metal  
745 concentration data. *Chem. Geol.* 324, 6-18.

746 Algeo, T.J., Tribovillard, N., 2009. Environmental analysis of

- 747 paleoceanographic systems based on molybdenum-uranium covariation.  
748 Chem. Geol. 268, 211-225.
- 749 Anbar, A., Duan, Y., Lyons, T.W., Arnold, G.L., Kendall, B., Creaser, R.A.,  
750 Kaufman, A.J., Gordon, G.W., Scott, C.T., Garvin, J., Buick, R., 2007. A  
751 whiff of oxygen before the Great Oxidation Event? Science 317 (5846),  
752 1903-1906.
- 753 Anbar, A.D., Knoll, A.H., 2002. Proterozoic ocean chemistry and evolution: a  
754 bioinorganic bridge? Science 297, 1137-1142.
- 755 Bowyer, F., Wood, R.A., Poulton, S.M., 2017. Controls on the evolution of  
756 Ediacaran metazoan ecosystems: A redox perspective. Geobiology 00,  
757 1-36.
- 758 Brocks, J.J., Jarrett, A.J.M., Sirantoine, E., Hallmann, C., Hoshino, Y.,  
759 Liyanage, T., 2017. The rise of algae in Cryogenian oceans and the  
760 emergence of animals. Nature 548, 578-581.
- 761 Butterfield, N.J., 2009. Oxygen, animals and oceanic ventilation: an  
762 alternative view. Geobiology 7, 1-7.
- 763 Campbell, I.H., Squire, R.J., 2010. The mountains that triggered the Late  
764 Neoproterozoic increase in oxygen: The Second Great Oxidation Event.  
765 Geochim. Cosmochim. Acta 74, 4187-4206.
- 766 Canfield, D.E., Thamdrup, B., 2009. Towards a consistent classification  
767 scheme for geochemical environments, or, why we wish the term  
768 'suboxic' would go away. Geobiology 7, 385-392.

- 769 Canfield, D.E., Glazer, A.N., Falkowski, P.G., 2010. The evolution and future  
770 of Earth's nitrogen cycle. *Science* 330, 192-196.
- 771 Canfield, D.E., Poulton, S.W., Knoll, A.H., Narbonne, G.M., Ross, G.,  
772 Goldberg, T., Strauss, H., 2008. Ferruginous conditions dominated later  
773 Neoproterozoic deep-water chemistry. *Science* 321, 949-952.
- 774 Canfield, D.E., Poulton, S.W., Narbonne, G.M., 2007. Late-Neoproterozoic  
775 deep-ocean oxygenation and the rise of animal life. *Science* 315, 92-95.
- 776 Canfield, D.E., Raiswell, R., Westrich, J.T., Reaves, C.M., Berner, R.A., 1986.  
777 The use of chromium reduction in the analysis of reduced inorganic  
778 sulfur in sediments and shales. *Chem. Geol.* 54, 149-155.
- 779 Chen, X., Ling, H.-F., Vance, D., Shields-Zhou, G.A., Zhu, M., Poulton, S.W.,  
780 Och, L.M., Jiang, S.Y., Li, D., Cremonese, L., Archer, C., 2015. Rise to  
781 modern levels of ocean oxygenation coincided with the Cambrian  
782 radiation of animals. *Nat. Commun.* 6.
- 783 Chen, Y., Diamond, C.W., Stüeken, E.E., Cai, C.F., Gill, B.C., Zhang, F.F.,  
784 Bates, S.M., Chu, X.L., Ding, Y., Lyons, T.W., 2019. Coupled evolution of  
785 nitrogen cycling and redoxcline dynamics on the Yangtze Block across  
786 the Ediacaran-Cambrian transition. *Geochim. Cosmochim. Acta* 257,  
787 243-265.
- 788 Clarkson, M.O., Poulton, S.W., Guilbaud, R., Wood, R.A., 2014. Assessing  
789 the utility of Fe/Al and Fe-speciation to record water column redox  
790 conditions in carbonate-rich sediments. *Chem. Geol.* 382, 111-122.

- 791 Cline, J.D., Kaplan, I.R., 1975. Isotopic fractionation of dissolved nitrate  
792 during denitrification in the eastern tropical North Pacific. *Mar. Chem.* 3,  
793 271-299.
- 794 Cremonese, L., Shields-Zhou, G., Struck, U., Ling, H.F., Och, L., Chen, X., Li,  
795 D., 2013. Marine biogeochemical cycling during the early Cambrian  
796 constrained by a nitrogen and organic carbon isotope study of the  
797 Xiaotan section, South China. *Precambrian Res.* 225, 148-165.
- 798 Cremonese, L., Shields-Zhou, G.A., Struck, U., Ling, H.-F., Och, L.M., 2014.  
799 Nitrogen and organic carbon isotope stratigraphy of the Yangtze Platform  
800 during the Ediacaran-Cambrian transition in South China. *Palaeogeogr.*  
801 *Palaeoclimatol. Palaeoecol.* 398, 165-186.
- 802 Doyle, K.A., Poulton, S.W., Newton, R.J., Podkovyrov, V.N., Bekker, A., 2018.  
803 Shallow water anoxia in the Mesoproterozoic ocean: Evidence from the  
804 Bashkir Meganticlinorium, Southern Urals. *Precambrian Res.* 317,  
805 196-210.
- 806 Feng, L., Li, C., Huang, J., Chang, H., Chu, X., 2014. A sulfate control on  
807 marine mid-depth euxinia on the early Cambrian (ca. 529-521 Ma)  
808 Yangtze platform, South China. *Precambrian Res.* 246, 123-133.
- 809 Gao, P., Liu, G., Jia, C., Ding, X., Chen, Z., Dong, Y., Zhao, X., Jiao, W., 2015.  
810 Evaluating rare earth elements as a proxy for oil–source correlation. A  
811 case study from Aer Sag, Erlian Basin, Northern China. *Org. Geochem.*  
812 87, 35-54.

- 813 Gao, P., Li, S., Lash, G.G., He, Z., Xiao, X., Zhang, D., Hao, Y., 2020.  
814 Silicification and Si cycling in a silica-rich ocean during the  
815 Ediacaran-Cambrian transition. *Chem. Geol.* 119787.
- 816 Godfrey, L.V., Falkowski, P.G., 2009. The cycling and redox state of nitrogen  
817 in the Archaean ocean. *Nat. Geosci.* 2, 725-729.
- 818 Godfrey, L.V., Poulton, S.W., Bebout, G.E., Fralick, P.W., 2013. Stability of the  
819 nitrogen cycle during development of sulfidic water in the redox-stratified  
820 late Paleoproterozoic ocean. *Geology* 41, 655-658.
- 821 Goldberg, T., Strauss, H., Guo, Q., Liu, C., 2007. Reconstructing marine  
822 redox conditions for the Early Cambrian Yangtze Platform: evidence from  
823 biogenic sulphur and organic carbon isotopes. *Palaeogeogr.*  
824 *Palaeoclimatol. Palaeoecol.* 254, 175-193.
- 825 Granger, J., Sigman, D.M., Lehmann, M.F., Tortell, P.D., 2008. Nitrogen and  
826 oxygen isotope fractionation during dissimilatory nitrate reduction by  
827 denitrifying bacteria. *Limnol. Oceanogr.* 53, 2533-2545.
- 828 Guilbaud, R., Slater, B.J., Poulton, S.W., Harvey, T.H.P., Brocks, J.J.,  
829 Nettersheim, B.J., Butterfield, N.J., 2018. Oxygen minimum zones in the  
830 early Cambrian ocean. *Geochem. Persp. Lett.* 6, 33-38.
- 831 Hadas, O., Altabet, M.A., Agnihotri, R., 2009. Seasonally varying nitrogen  
832 isotope biogeochemistry of particulate organic matter (POM) in Lake  
833 Kinneret, Israel. *Limnol. Oceanogr.* 54, 75-85.
- 834 Hammarlund, E.U., Gaines, R.R., Prokopenko, M.G., Qi, C., Hou, X.G.,

- 835 Canfield, D.E., 2017. Early Cambrian oxygen minimum zone-like  
836 conditions at Chengjiang. *Earth Planet. Sci. Lett.* 475, 160-168.
- 837 He, T., Zhu, M., Mills, B.J.W., Wynn, P.M., Zhuravlev, A.Y., Tostevin, R.,  
838 Pogge von Strandmann, P.A.E., Yang, A., Poulton, S.W., Shields, G.A.,  
839 2019. Possible links between extreme oxygen perturbations and the  
840 Cambrian radiation of animals. *Nat. Geosci.* 12, 468-474.
- 841 Higgins, M.B., Robinson, R.S., Husson, J.M., Carter, S.J., Pearson, A., 2012.  
842 Dominant eukaryotic export production during ocean anoxic events  
843 reflects the importance of recycled  $\text{NH}_4^+$ . *Proc. Natl. Acad. Sci. U. S. A.*  
844 109, 2269-2274.
- 845 Huang, Z.H., Zhang, S.W., 1988. Lithofacies paleogeography of Cambrian  
846 Zhejiang Province. *Lithofacies Paleogeogr.* 33, 13-21 (in Chinese).
- 847 Jiang, G.Q., Wang, X.Q., Shi, X.Y., Xiao, S.H., Zhang, S.H., Dong, J., 2012.  
848 The origin of decoupled carbonate and organic carbon isotope  
849 signatures in the early Cambrian (ca. 542-520 Ma) Yangtze platform.  
850 *Earth Planet. Sci. Lett.* 317, 96-110.
- 851 Jiang, S.Y., Chen, Y.Q., Ling, H.F., Yang, J.H., Feng, H.Z., Ni, P., 2006.  
852 Trace-and rare-earth element geochemistry and Pb-Pb dating of black  
853 shales and intercalated Ni-Mo-PGE-Au sulfide ores in Lower Cambrian  
854 strata, Yangtze Platform, South China. *Miner. Depos.* 41, 453-467.
- 855 Jiang, S.Y., Pi, D.H., Heubeck, C., Frimmel, H., Liu, Y.P., Deng, H.L., Ling,  
856 H.F., Yang, J.H., 2009. Early Cambrian ocean anoxia in south China.

- 857 Nature 459, E5-E6.
- 858 Jin, C., Li, C., Algeo, T.J., Planavsky, N.J., Cui, H., Yang, X., Zhao, Y., Zhang,  
859 X., Xie, S., 2016. A highly redox-heterogeneous ocean in South China  
860 during the early Cambrian (~529-514 Ma): implications for  
861 biota-environment co-evolution. *Earth Planet. Sci. Lett.* 441, 38-51.
- 862 Kipp, M.A., Stüeken, E.E., Yun, M., Bekker, A., Buick, R., 2018. Pervasive  
863 aerobic nitrogen cycling in the surface ocean across the  
864 Paleoproterozoic Era. *Earth Planet. Sci. Lett.* 500, 117-126.
- 865 Křibek, B., Sýkorová, I., Pašava, J., Machovič, V., 2007. Organic  
866 geochemistry and petrology of barren and Mo-Ni-PGE mineralized  
867 marine black shales of the Lower Cambrian Niutitang Formation (South  
868 China). *Int. J. Coal Geol.* 72, 240-256.
- 869 Koehler, M.C., Stüeken, E.E., Hillier, S., Prave, A.R., 2019. Limitation of fixed  
870 nitrogen and deepening of the carbonate-compensation depth through  
871 the Hirnantian at Dob's Linn, Scotland. *Palaeogeogr. Palaeoclimatol.*  
872 *Palaeoecol.* 534, 109321.
- 873 Koehler, M.C., Stüeken, E.E., Kipp, M.A., Buick, R., Knoll, A.H., 2017. Spatial  
874 and temporal trends in Precambrian nitrogen cycling: a Mesoproterozoic  
875 offshore nitrate minimum. *Geochim. Cosmochim. Acta* 198, 315-337.
- 876 Krause, A.J., Mills, B.J.W., Zhang, S., Planavsky, N.J., Lenton, T.M.,  
877 Poulton, S.W., 2018. Stepwise oxygenation of the Paleozoic atmosphere.  
878 *Nat. Commun.* 9, 4081.

- 879 Lam, P., Lavik, G., Jensen, M.M., van de Vossenberg, J., Schmid, M.,  
880 Woebken, D., Dimitri Gutiérrez, D., Amann, R., Jetten, M.S.M., Kuypers,  
881 M.M.M., 2009. Revising the nitrogen cycle in the Peruvian oxygen  
882 minimum zone. *Proc. Natl. Acad. Sci. U. S. A.* 106, 4752-4757.
- 883 Lehmann, B., Nägler, T.F., Holland, H.D., Wille, M., Mao, J.W., Pan, J.Y., Ma,  
884 D.S., Dulski, P., 2007. Highly metalliferous carbonaceous shale and  
885 Early Cambrian seawater. *Geology* 35, 403-406.
- 886 Lenton, T.M., Boyle, R.A., Poulton, S.W., Shields-Zhou, G.A., Butterfield, N.J.,  
887 2014. Co-evolution of eukaryotes and ocean oxygenation in the  
888 Neoproterozoic era. *Nature Geosci.* 7, 257-265.
- 889 Li C., Jin C., Planavsky N. J., Algeo T. J., Cheng M., Yang X., Zhao Y., Xie S.,  
890 2017. Coupled oceanic oxygenation and metazoan diversification during  
891 the early-middle Cambrian? *Geology* 45, 743-746.
- 892 Li, C., Cheng, M., Zhu, M., Lyons, T.W., 2018. Heterogeneous and dynamic  
893 marine shelf oxygenation and coupled early animal evolution. *Emerg.*  
894 *Top. Life. Sci.* 28, 279-288.
- 895 Li, C., Love, G.D., Lyons, T.W., Fike, D.A., Sessions, A.L., Chu, X., 2010. A  
896 stratified redox model for the Ediacaran ocean. *Science* 328, 80-83.
- 897 Logan, G.A., Hayes, J., Hieshima, G.B., Summons, R.E., 1995. Terminal  
898 Proterozoic re-organization of biogeochemical cycles. *Nature* 376, 53-56.
- 899 Luo, H.L., Jiang, Z.W., Tang, L.D., 1994. Stratotype Section for Lower  
900 Cambrian Stages in China. Yunnan Science and Technology Press,

- 901 Kunming, China (in Chinese with English abstract).
- 902 Magnall, J.M., Gleeson, S.A., Poulton, S.W., Gordon, G.W., Paradis, S., 2018.
- 903 Links between seawater paleoredox and the formation of
- 904 sediment-hosted massive sulphide (SHMS) deposits-Fe speciation and
- 905 Mo isotope constraints from Late Devonian mudstones. *Chem. Geol.* 490,
- 906 45-60.
- 907 McLennan, S.M., 2001. Relationships between the trace element composition
- 908 of sedimentary rocks and upper continental crust. *Geochemistry,*
- 909 *Geophysics, Geosystems* 2, paper number 2000GC000109.
- 910 Merdith, A.S., Collins, A.S., Williams, S.E., Pisarevsky, S., Foden, J.F.,
- 911 Archibald, D.A., Blades, M.L., Alessio, B.L., Armistead, S., Plavsa, D.,
- 912 Clark, C., Müller, R.D., 2017. A full-plate global reconstruction of the
- 913 Neoproterozoic. *Gondwana Res.* 50, 84-134.
- 914 Och, L.M., Cremonese, L., Shields-Zhou, G.A., Poulton, S.W., Struck, U.,
- 915 Ling, H., Li, D., Chen, X., Manning, C., Thirlwall, M., Strauss, H., Zhu, M.,
- 916 2016. Palaeoceanographic controls on spatial redox distribution over the
- 917 Yangtze Platform during the Ediacaran–Cambrian transition.
- 918 *Sedimentology.* 63, 378-410.
- 919 Och, L.M., Shields-Zhou, G.A., Poulton, S.W., Manning, C., Thirlwall, M.F., Li,
- 920 D., Chen, X., Ling, H., Osborn, T., Cremonese, L., 2013. Redox changes
- 921 in Early Cambrian black shales at Xiaotan section, Yunnan Province,
- 922 South China. *Precambrian Res.* 225, 166-189.

- 923 Papineau, D., Purohit, R., Goldberg, T., Pi, D., Shields, G.A., Bhu, H., Steele,  
924 A., Fogel, M.L., 2009. High primary productivity and nitrogen cycling after  
925 the Paleoproterozoic phosphogenic event in the Aravalli supergroup,  
926 India. *Precambrian Res.* 171, 37-56.
- 927 Pennock, J.R., Velinsky, D.J., Ludlam, J.M., Sharp, J.H., Fogel, M.L., 1996.  
928 Isotopic fractionation of ammonium and nitrate during uptake by  
929 *Skeletonema costatum*: implications for  $\delta^{15}\text{N}$  dynamics under bloom  
930 conditions. *Limnol. Oceanogr.* 41, 451-459.
- 931 Pi, D.H., Liu, C.Q., Shields-Zhou, G.A., Jiang, S.Y., 2013. Trace and rare  
932 earth element geochemistry of black shale and kerogen in the early  
933 Cambrian Niutitang Formation in Guizhou province, South China:  
934 constraints for redox environments and origin of metal enrichments.  
935 *Precambrian Res.* 225, 218-229.
- 936 Poulton, S.W., Canfield, D.E., 2005. Development of a sequential extraction  
937 procedure for iron: implications for iron partitioning in continentally  
938 derived particulates. *Chem. Geol.* 214, 209-221.
- 939 Poulton, S.W., Canfield, D.E., 2011. Ferruginous conditions: a dominant  
940 feature of the ocean through Earth's history. *Elements* 7, 107-112.
- 941 Poulton, S.W., Fralick, P.W., Canfield, D.E., 2010. Spatial variability in  
942 oceanic redox structure 1.8 billion years ago. *Nat. Geosci.* 3, 486-490.
- 943 Poulton, S.W., Fralick, P.W., Canfield, D.E., 2004. The transition to a  
944 sulphidic ocean approximately 1.84 billion years ago. *Nature* 431,

945 173-177.

946 Poulton, S.W., Raiswell, R., 2002. The low-temperature geochemical cycle of  
947 iron: from continental fluxes to marine sediment deposition. *Am. J. Sci.*  
948 302, 774-805.

949 Raiswell, R., Canfield, D.E., 2012. The iron biogeochemical cycle past and  
950 present. *Geochem. Persp.* 1, 1-220.

951 Raiswell, R., Hardisty, D.S., Lyons, T.W., Canfield, D.E., Owens, J.D.,  
952 Planavsky, N.J., Poulton, S.W., Reinhard, C.T., 2018. The iron  
953 paleoredox proxies: a guide to the pitfalls, problems and proper practice.  
954 *Am. J. Sci.* 318, 491-526.

955 Sahoo, S.K., Planavsky, N.J., Kendall, B., Wang, X.Q., Shi, X.Y., Scott, C.,  
956 Anbar, A.D., Lyons, T.W., Jiang, G.Q., 2012. Ocean oxygenation in the  
957 wake of the Marinoan glaciation. *Nature* 489, 546-549.

958 Scholz, F., McManus, J., Sommer, S., 2013. The manganese and iron shuttle  
959 in a modern euxinic basin and implications for molybdenum cycling at  
960 euxinic ocean margins. *Chem. Geol.* 355, 56-68.

961 Scott, C., Lyons, T. W., Bekker, A., Shen, Y., Poulton, S. W., Chu, X., Anbar, A.  
962 D., 2008. Tracing the stepwise oxygenation of the Proterozoic ocean.  
963 *Nature* 452, 456-459.

964 Scott, C., Lyons, T.W., 2012. Contrasting molybdenum cycling and isotopic  
965 properties in euxinic versus non-euxinic sediments and sedimentary  
966 rocks: refining the paleoproxies. *Chem. Geol.* 324, 19-27.

- 967 Sperling, E.A., Wolock, C.J., Morgan, A.S., Gill, B.C., Kunzmann, M.,  
968 Halverson, G.P., Macdonald, F.A., Knoll, A.H., Johnston, D.T., 2015.  
969 Statistical analysis of iron geochemical data suggests limited late  
970 Proterozoic oxygenation. *Nature* 523, 451-454.
- 971 Steiner, M., Wallis, E., Erdtmann, B.D., Zhao, Y.L., Yang, R.D., 2001.  
972 Submarine-hydrothermal exhalative ore layers in black shales from  
973 South China and associated fossils-insights into a Lower Cambrian  
974 facies and bio-evolution. *Palaeogeogr. Palaeoclimatol. Palaeoecol.* 169,  
975 165-191.
- 976 Stüeken, E.E., 2013. A test of the nitrogen-limitation hypothesis for retarded  
977 eukaryote radiation: nitrogen isotopes across a Mesoproterozoic basinal  
978 profile. *Geochim. Cosmochim. Acta* 120, 121-139.
- 979 Stüeken, E.E., Kipp, M.A., Koehler, M.C., Buick, R., 2016. The evolution of  
980 earth's biogeochemical nitrogen cycle. *Earth Sci. Rev.* 160, 220-239.
- 981 Tesdal, J.E., Galbraith, E.D., Kienast, M., 2013. Nitrogen isotopes in bulk  
982 marine sediment: linking seafloor observations with subseafloor records.  
983 *Biogeosciences* 10, 101-118.
- 984 Thomazo, C., Ader, M., Phillippot, P., 2011. Extreme <sup>15</sup>N enrichment in  
985 2.72-Gyr-old sediments: evidence for a turning point in the nitrogen cycle.  
986 *Geobiology* 9, 107-120.
- 987 Tostevin, R., Wood, R.A., Shields, G.A., Poulton, S.W., Guilbaud, R., Bowyer,  
988 F., Penny, A.M., He, T., Curtis, A., Hoffmann, K.H., Clarkson, M.O., 2016.

- 989 Low-oxygen waters limited habitable space for early animals. *Nat.*  
990 *Commun.* 7, 12818.
- 991 Tribovillard, N., Algeo, T.J., Lyons, T., Riboulleau, A., 2006. Trace metals as  
992 paleoredox and paleoproductivity proxies: an update. *Chem. Geol.* 232,  
993 12-32.
- 994 Vinther, J., Stein, M., Longrich, N.R., Harper, D.A.T., 2014. A  
995 suspension-feeding anomalocarid from the Early Cambrian. *Nature* 507,  
996 496-499.
- 997 Wang, D., Ling, H.F., Struck, U., Zhu, X.K., Zhu, M., He, T., Yang, B., Gamper,  
998 A., Shields G. A., 2018. Coupling of ocean redox and animal evolution  
999 during the Ediacaran-Cambrian transition. *Nat. Commun.* 9, 2575.
- 1000 Wang, D., Struckb, U., Ling, H.F., Guo, Q.J., Graham, A., Zhou, S., Zhu, M.Y.,  
1001 Yao, S.P., 2015. Marine redox variations and nitrogen cycle of the early  
1002 Cambrian southern margin of the Yangtze Platform, South China:  
1003 evidence from nitrogen and organic carbon isotopes. *Precambrian Res.*  
1004 267, 209-226.
- 1005 Wang, J., Chen, D., Yan, D., Wei, H., Xiang, L., 2012. Evolution from an  
1006 anoxic to oxic deep ocean during the Ediacaran-Cambrian transition and  
1007 implications for bioradiation. *Chem. Geol.* 306-307, 129-138.
- 1008 Wen, H. J., Fan, H. F., Zhang, Y. X., Cloquet, C., Carignan, J., 2015.  
1009 Reconstruction of early Cambrian ocean chemistry from Mo isotopes.  
1010 *Geochim. Cosmochim. Acta* 164, 1-16.

- 1011 Wille, M., Nägler, T.F., Lehmann, B., Schröder, S., Kramers, J.D., 2008.  
1012 Hydrogen sulphide release to surface waters at the  
1013 Precambrian/Cambrian boundary. *Nature* 453, 767-769.
- 1014 Wood, R., Liu, A.G., Bowyer, F., Wilby, P.R., Dunn, F.S., Kenchington, C.G.,  
1015 Cuthill, J.F.H., Mitchell, E.G., Penny, A., 2019. Integrated records of  
1016 environmental change and evolution challenge the Cambrian Explosion.  
1017 *Nat. Ecol. Evol.* 3, 528-538.
- 1018 Xiang, L., Schoepfer, S.D., Zhang, H., Cao, C.Q., Shen, S.Z., 2018. Evolution  
1019 of primary producers and productivity across the Ediacaran-Cambrian  
1020 transition. *Precambrian Res.* 313, 68-77.
- 1021 Xu, D.T., Wang, X.Q., Shi, X.Y., Tang, D.J., Zhao, X.K., Feng, L.J., Song,  
1022 H.Y., 2020. Nitrogen cycle perturbations linked to metazoan  
1023 diversification during the early Cambrian. *Palaeogeogr. Palaeoclimatol.*  
1024 *Palaeoecol.* 538, 109392.
- 1025 Xu, L.G., Lehmann, B., Mao, J.W., Nägler, T.F., Neubert, N., Böttcher, M.E.,  
1026 Escher, P., 2012. Mo isotope and trace element patterns of Lower  
1027 Cambrian black shales in South China: multi-proxy constraints on the  
1028 paleoenvironment. *Chem. Geol.* 318-319, 45-59.
- 1029 Xu, L.G., Lehmann, B., Mao, J.W., Qu, W.J., Du, A.D., 2011. Re-Os age of  
1030 polymetallic Ni–Mo–PGE–Au mineralization in early Cambrian black  
1031 shales of South China—a reassessment. *Econ. Geol.* 106, 511-522.
- 1032 Xue, Y.S., Yu, C.L., 1979. Petrology and depositional environment analysis of

- 1033 Hetang Formation, Lower Cambrian, western Zhejiang and eastern  
1034 Jiangxi. *Acta Stratigraphica Sin.* 3, 283-295 (in Chinese).
- 1035 Yin, R., Xu, L., Lehmann, B., Lepak, R.F., Hurley, J.P., Mao, J.W., Feng, X.,  
1036 Hu, R., 2017. Anomalous mercury enrichment in Early Cambrian black  
1037 shales of South China: Mercury isotopes indicate a seawater source.  
1038 *Chem. Geol.* 467, 159-167.
- 1039 Zerkle, A.L., Poulton, S.W., Newton, R.J, Mettam, C., Claire, M.W., Bekker, A.,  
1040 Junium, C.K., 2017. Onset of the aerobic nitrogen cycle during the Great  
1041 Oxidation Event. *Nature* 542, 392-512
- 1042 Zhang, J., Fan, T., Zhang, Y., Lash, G.G., Li, Y., Wu, Y., 2017. Heterogenous  
1043 oceanic redox conditions through the Ediacaran-Cambrian boundary  
1044 limited the metazoan zonation. *Sci. Rep.* 7, 8550.
- 1045 Zhang, X., Sigman, D.M., Morel, F.M., Kraepiel, A.M., 2014. Nitrogen isotope  
1046 fractionation by alternative nitrogenases and past ocean anoxia. *Proc.*  
1047 *Natl. Acad. Sci.* 111, 4782-4787.
- 1048 Zhang, Z., Li, C., Cheng, M., Algeo, T. J., Jin, C., Tang, F., Huang, J., 2018.  
1049 Evidence for highly complex redox conditions and strong water-column  
1050 stratification in an early Cambrian continental-margin sea. *Geochemistry,*  
1051 *Geophysics, Geosystems*, 19, 2397-2410.
- 1052 Zhu, M., Strauss, H., Shields, G.A., 2007. From snowball earth to the  
1053 Cambrian bioradiation: calibration of Ediacaran-Cambrian earth history in  
1054 South China. *Palaeogeogr. Palaeoclimatol. Palaeoecol.* 254, 1-6.

1055 Zhu, M.Y., 2010. The origin and Cambrian explosion of animals: Fossil  
1056 evidence from China. *Acta Palaeontol. Sin.* 49, 269-287 (in Chinese with  
1057 English abstract).

1058 Zhuravlev, A. Yu., Wood, R. A., 1996. Anoxia as the cause of the mid-Early  
1059 Cambrian (Botomian) extinction event. *Geology.* 24, 311-314.

1060

1061

1062

1063

1064

1065

1066

1067

1068

1069

1070

1071

1072

1073

1074

1075

1076

1077 Figure captions

1078 Fig. 1, Simplified geological map of the Yangtze Platform (after [Steiner et al.,](#)  
1079 [2001](#); [Jiang et al., 2012](#)) and stratigraphic column of outer-shelf  
1080 Zhongnancun section. Sections: 1-Xiaotan, 2-Meishucun, 3-CJ2 drill  
1081 core, 4-Jinsha, 5-Dingtai, 6-Zhongnancun, 7-Sancha, 8-Yangjiaping,  
1082 9-Wengan, 10-Songtao, 11-Longbizui, 12-zk2012 drill core, 13-Lijiatuo,  
1083 14-Yuanjia, 15-Siduping, 16-Hejiapu, 17-Silikou, 18-Yanjia, 19-Chunye  
1084 1 drill core.

1085 Fig. 2, Stratigraphic distribution of Fe species, TOC contents, TN contents,  
1086 Mo, U and V concentrations, Mo/TOC ratios,  $\delta^{13}\text{C}_{\text{org}}$  and  $\delta^{15}\text{N}_{\text{sed}}$  values  
1087 at the Zhongnancun section (reference  $\delta^{15}\text{N}_{\text{sed}}$  data at the  
1088 Zhongnancun section from [Zhang et al., 2017](#) with orange symbol).  
1089 Gray vertical lines represent the divisions between oxic ( $\text{Fe}_{\text{HR}}/\text{Fe}_{\text{T}} <$   
1090  $0.22$ ; [Poulton and Raiswell, 2002](#)), equivocal ( $\text{Fe}_{\text{HR}}/\text{Fe}_{\text{T}} = 0.22-0.38$ ;  
1091 [Poulton and Canfield, 2011](#)) and anoxic conditions ( $\text{Fe}_{\text{HR}}/\text{Fe}_{\text{T}} > 0.38$ ;  
1092 [Poulton and Raiswell, 2002](#)), and between ferruginous and euxinic  
1093 conditions ( $\text{Fe}_{\text{py}}/\text{Fe}_{\text{HR}}=0.7$ ; [Poulton and Canfield, 2011](#)).

1094 Fig. 3, Crossplot of Mo versus TOC (a) and U versus TOC. A good positive  
1095 correlation of Mo and TOC content can be found in samples from  
1096 Interval 3, but the lack of correlation between Mo and TOC for Interval  
1097 1 and 2 suggests that the black shales with higher Mo contents from  
1098 Interval 1 and 2 are deposited in euxinic/anoxic environments and the

1099 black shales with low Mo concentration from Interval 3 are deposited in  
1100 oxic/suboxic environments. The content of U and TOC decreased  
1101 gradually from Interval 1 to Interval 3 and the U-TOC correlation  
1102 becomes stronger, suggesting that the redox condition evolved from  
1103 euxinic to oxic/suboxic.

1104 Fig. 4, Crossplots of  $Mo_{EF}$  versus  $U_{EF}$  with enrichment factors normalized to  
1105 AUCC (McLennan, 2001). The trend lines are modified from Algeo and  
1106 Tribovillard (2009). The data includes the section of this study and the  
1107 compiled data from multiple sections (CJ2 from Hammarlund et al.,  
1108 2017, Jinsha and Wengan from Jin et al., 2016, Dingtai from Xu et al.,  
1109 2012), all of the data correspond to the Cambrian Stage 2 to 3.

1110 Fig. 5, Spatio-temporal variations in watermass redox conditions from  
1111 inner-shelf to basin environment. The redox conditions of Xiaotan (Och  
1112 et al., 2013), CJ2 drill core (Hammarlund et al., 2017), Jinsha (Jin et al.,  
1113 2016), Wengan (Jin et al., 2016), Songtao (Goldberg et al., 2007; Guo  
1114 et al., 2007; Canfield et al., 2008), Longbizui (Wang et al., 2012),  
1115 Silikou (Zhang et al., 2018), Chunye1 drill core (Xiang et al., 2018)  
1116 sections are reconstructed from Fe speciation data; the redox  
1117 conditions of Sancha and Yuanjia are reconstructed from  $\delta^{13}C_{org}$ ,  
1118  $\delta^{15}N_{sed}$  and Mo data (Wang et al., 2015).

1119 Fig. 6, The biogeochemical nitrogen cycle. Elements in parentheses are used  
1120 as co-factors in enzymes and  $\epsilon$  is the fractionation factor (‰) related to

1121 the metabolic process ( $\epsilon \approx \delta^{15}\text{N}_{\text{product}} - \delta^{15}\text{N}_{\text{reactant}}$ ). Adapted from  
1122 [Stüeken et al. \(2016\)](#).

1123 Fig. 7, Nitrogen isotope chemostratigraphy of Xiaotan section ([Cremonese et](#)  
1124 [al., 2013](#)), CJ2 drill core ([Hammarlund et al., 2017](#)), Zhongnancun  
1125 section (this study), Sancha section ([Wang et al., 2015](#)), Siduping and  
1126 Hejiapu sections ([Xu et al., 2020](#)), Longbizui section ([Cremonese et al.,](#)  
1127 [2014](#)), zk2012 drill core ([Chen et al., 2019](#)), Lijiatuo section  
1128 ([Cremonese et al., 2014](#)), Yuanjia section ([Wang et al., 2015](#)), Silikou  
1129 section ([Zhang et al., 2018](#)), Yanjia section ([Wang et al., 2018](#)) and  
1130 Chunye1 drill core ([Xiang et al., 2018](#)).

1131 Fig. 8, Schematic of the proposed nitrogen cycle in the early Cambrian  
1132 Yangtze ocean during late Stage 2 (a) and early-middle Stage 3 (b).

1133 Fig. 9,  $\delta^{15}\text{N}_{\text{sed}}$  plotted against  $\delta^{13}\text{C}_{\text{org}}$  for the multiple sections in the Yangtze  
1134 Block, the plot only includes those samples corresponding to anoxic  
1135 conditions during the early-middle Cambrian Stage 3. The data of shelf  
1136 sections include Xiaotan section ([Cremonese et al., 2013](#)), CJ2 drill  
1137 core ([Hammarlund et al., 2017](#)), Zhongnancun section (this study) and  
1138 Sancha section ([Wang et al., 2015](#)). The data of slope-basin sections  
1139 include Siduping and Hejiapu sections ([Xu et al., 2020](#)), Longbizui  
1140 section ([Cremonese et al., 2014](#)), zk2012 drill core ([Chen et al., 2019](#)),  
1141 Lijiatuo section ([Cremonese et al., 2014](#)) and Yuanjia section ([Wang et](#)  
1142 [al., 2015](#)).

1143 Fig. 10, Nitrogen isotope distributions of modern surface sediments ([Testal et](#)  
1144 [al., 2013](#)) and early Cambrian Yangtze Block, South China (ca. 521-514  
1145 Ma).

1146

1147

1148

1149

1150 Table captions

1151 Table S1: Geochemical data for studied samples from Niutitang Formation at  
1152 Zhongnancun section, South China.

1153 Table S2: Fe speciation data for early Cambrian successions in the Yangtze  
1154 Block.

1155 Table S3:  $\delta^{15}\text{N}$  and  $\delta^{13}\text{C}_{\text{org}}$  values for early Cambrian successions in the  
1156 Yangtze Block.

1157

1158

1159

1160

1161

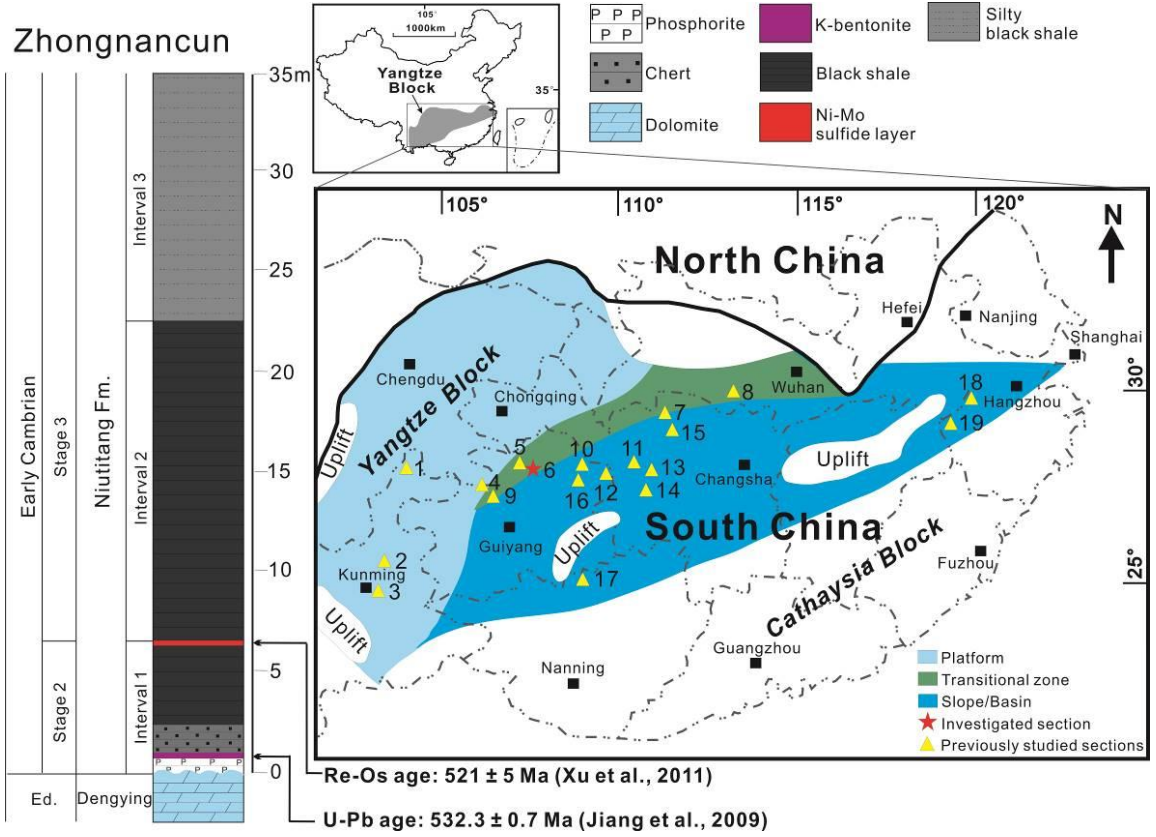
1162

1163

1164

1165

1166



1167

1168

1169

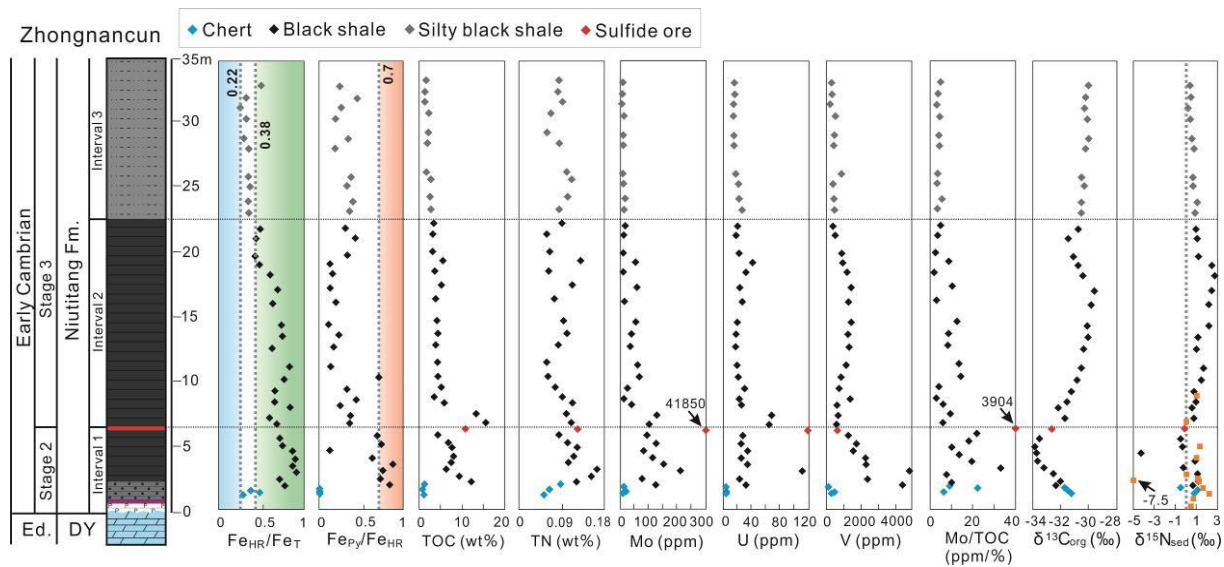
1170

1171

1172

1173

1174



1175

1176

1177

1178

1179

1180

1181

1182

1183

1184

1185

1186

1187

1188

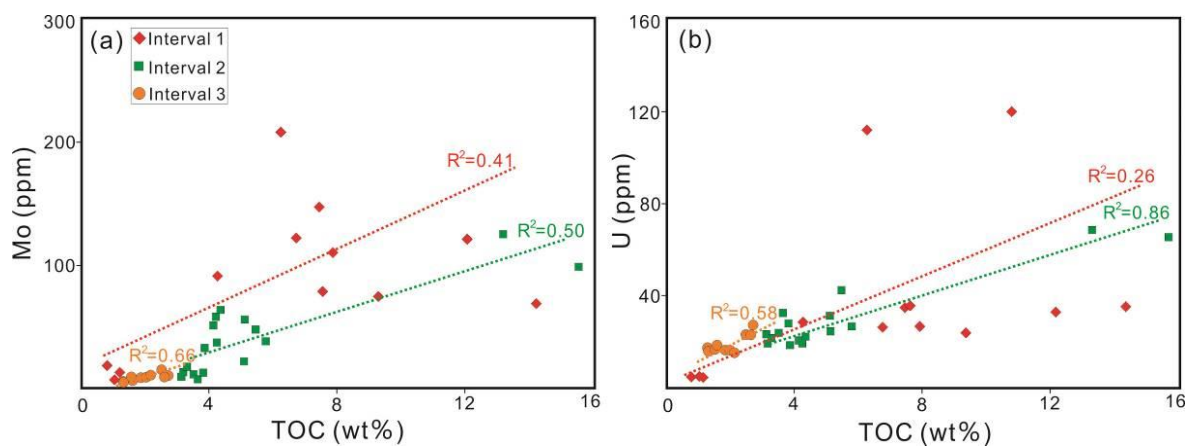
1189

1190

1191

1192

1193



1194

1195

1196

1197

1198

1199

1200

1201

1202

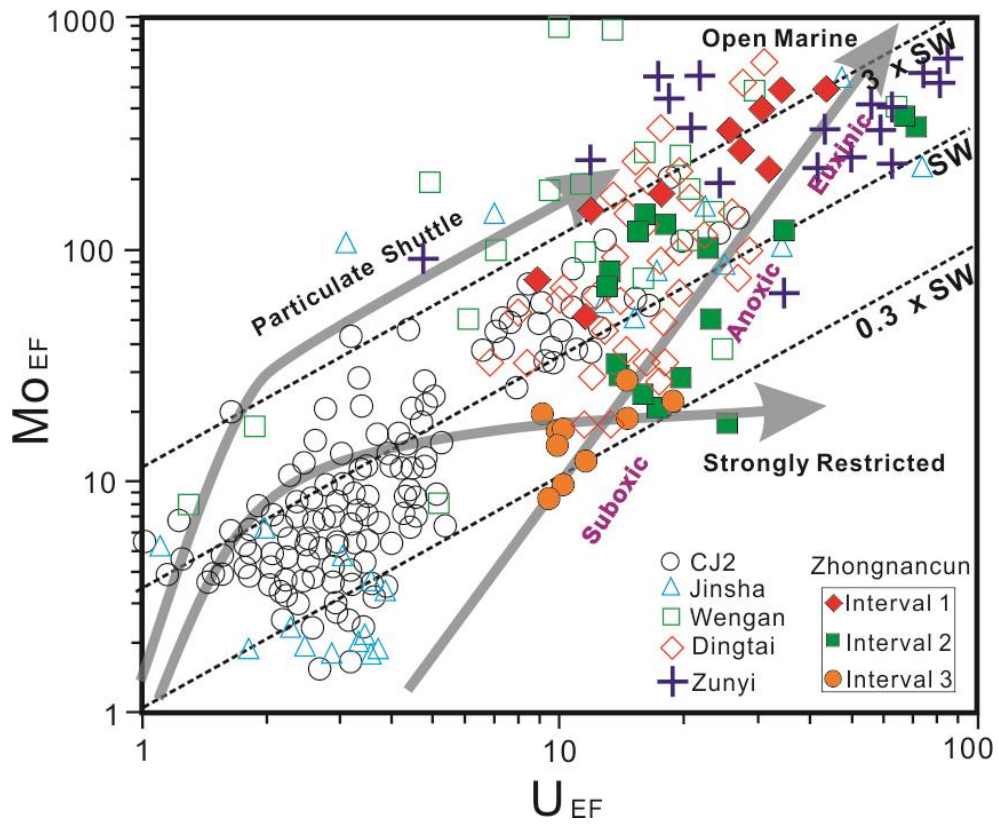
1203

1204

1205

1206

1207



1208

1209

1210

1211

1212

1213

1214

1215

1216

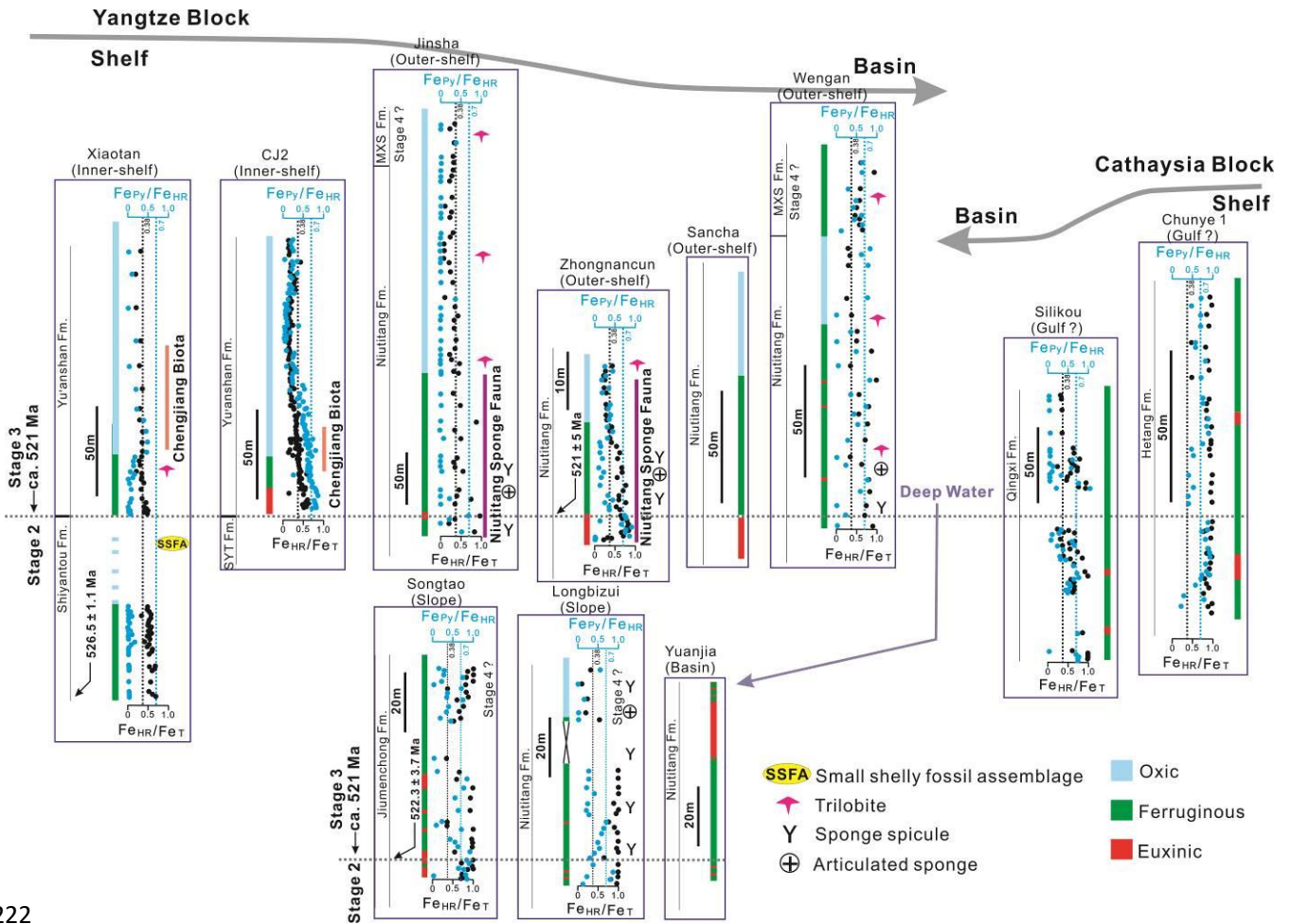
1217

1218

1219

1220

1221



1222

1223

1224

1225

1226

1227

1228

1229

1230

1231

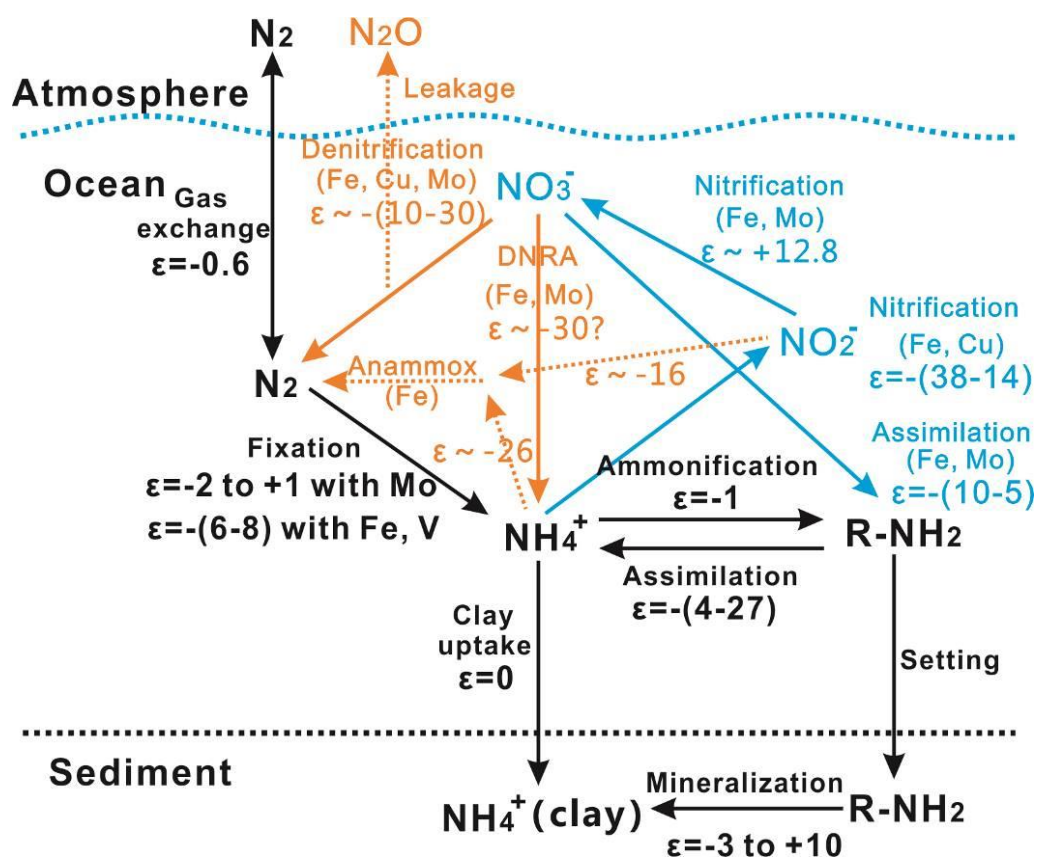
1232

1233

1234

1235

1236



1237

1238

1239

1240

1241

1242

1243

1244

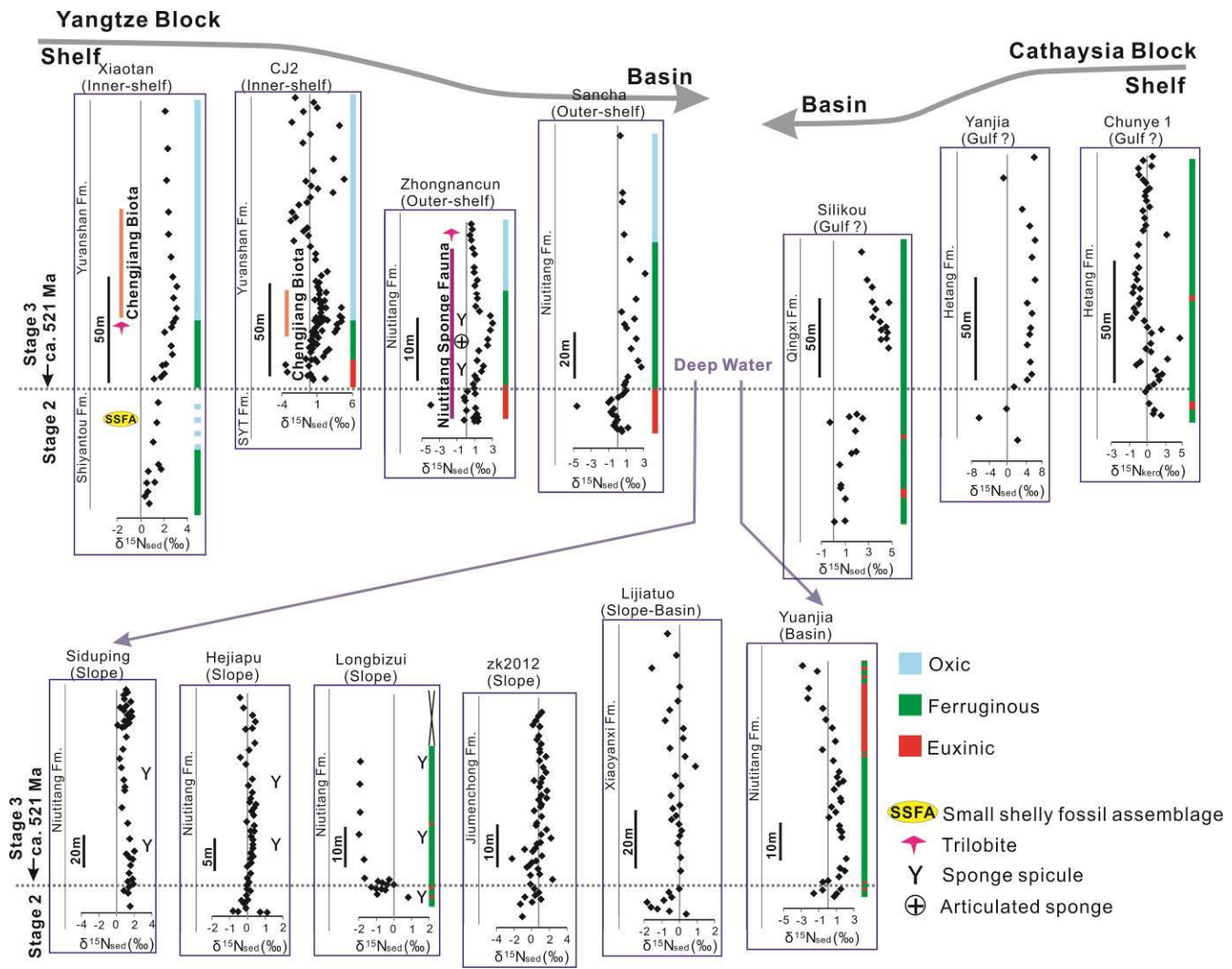
1245

1246

1247

1248

1249



1250

1251

1252

1253

1254

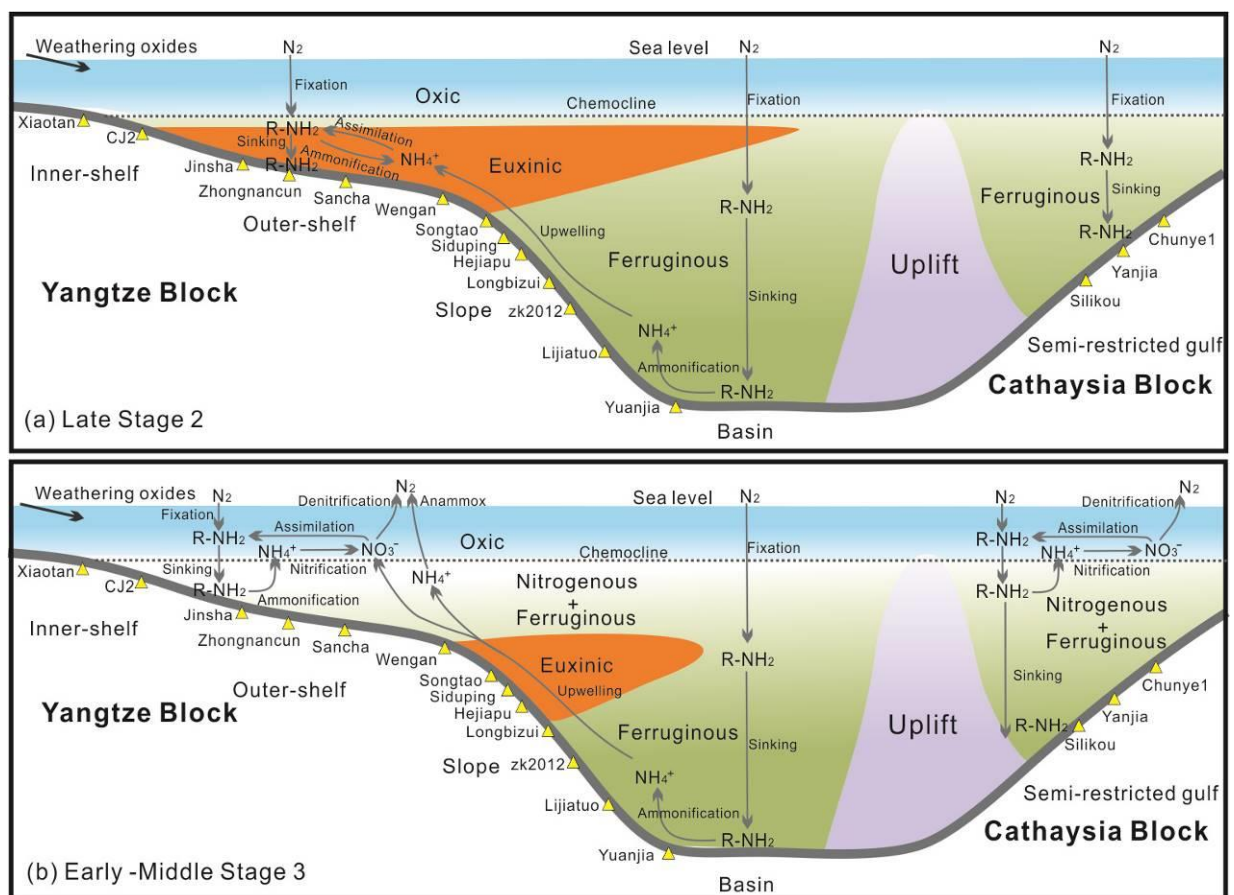
1255

1256

1257

1258

1259



1260

1261

1262

1263

1264

1265

1266

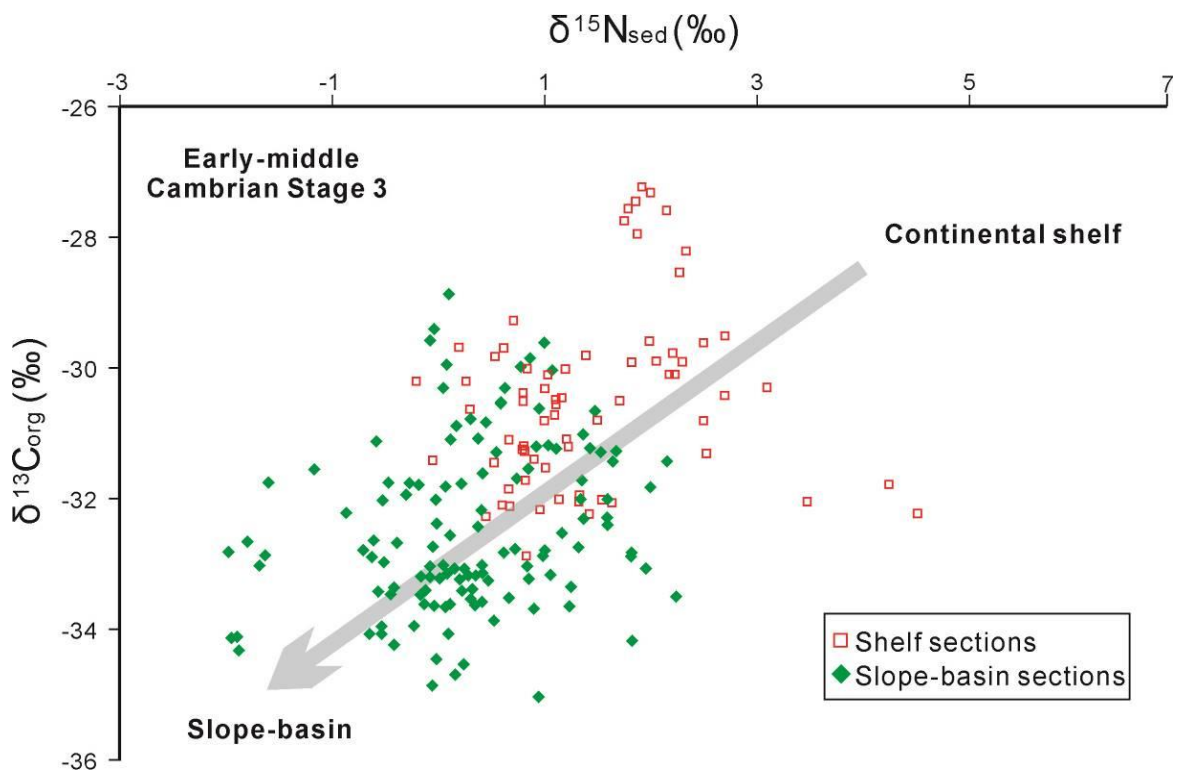
1267

1268

1269

1270

1271



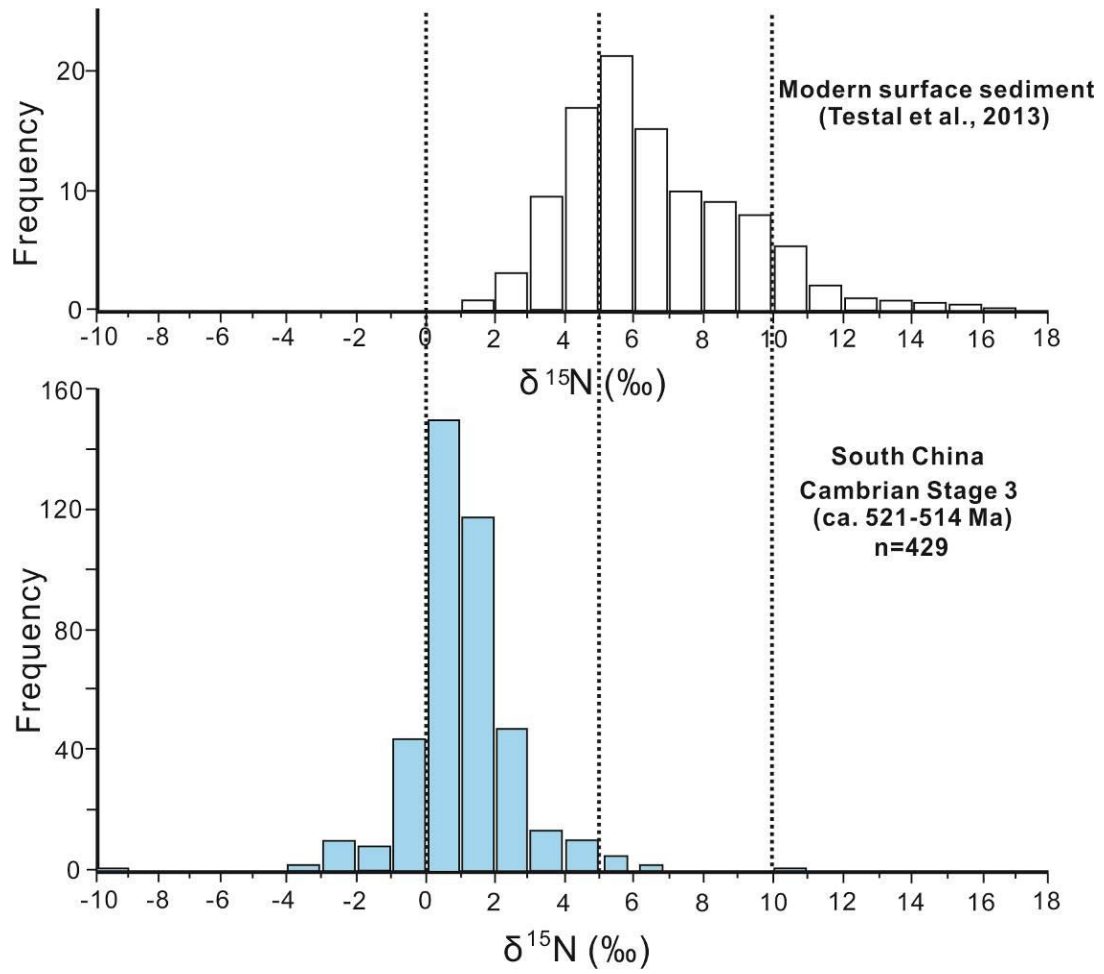
1272

1273

1274

1275

1276



1277

1278